Published for SISSA by Springer

Received: *March 19, 2020*
Revised: *May 13, 2020*
Accepted: *July 6, 2020*
Published: *August 12, 2020*

JHEP08(2020)052

Dark-matter-spin effects at future e^+e^- colliders

Bohdan Grzadkowski, Michal Iglicki, Krzysztof Mekala and Aleksander Filip Zarnecki

Faculty of Physics, University of Warsaw,
Pasteura 5, 02-093 Warsaw, Poland

E-mail: bohdan.grzadkowski@fuw.edu.pl, michal.iglicki@fuw.edu.pl, k.mekala@student.uw.edu.pl, filip.zarnecki@fuw.edu.pl

Abstract: We discuss the possibility to detect spin 0, 1 and 1/2 dark matter (DM) at future e^+e^- colliders. The models considered here are simple, consistent and renormalizable field theories that provide correct DM abundance and satisfy direct detection, indirect detection and collider constraints. The intention of this paper was to verify to what extent it might be possible to disentangle models of different DM spins by the measurement of the cross section for $e^+e^- \to Z + \cdots$ at future e^+e^- colliders. We specialize to the case of the ILC operating at $\sqrt{s} = 250\,\text{GeV}$, however our results apply as well for the FCC-ee and the CEPC colliders. For each model the cross section maximized with respect to parameters was calculated and compared to the expected 95% CL cross-section limits estimated for the ILC. It turned out that near the $2m_{\text{DM}} \simeq m_{1,2}$ resonances, where m_1 and m_2 are the SM Higgs boson and a non-standard Higgs boson masses, respectively, there exist substantial regions where the models are testable. A special attention has been payed to calculation of the cross section in the region where $m_1 \simeq m_2$.

Keywords: Beyond Standard Model, Dark matter, e^+-e^- Experiments

ArXiv ePrint: 2003.06719

https://doi.org/10.1007/JHEP08(2020)052

Contents

1 Introduction

In spite of the Higgs-boson discovery at CERN's Large Hadron Collider (LHC) by the ATLAS [1] and CMS [2] collaborations, the underlying theory of fundamental interactions is still missing since the Standard Model (SM) does not provide a candidate for dark matter (DM), while its existence has been confirmed by many independent experiments (see e.g. [3–11]). In this project we are going to discuss minimal extensions of the SM that describe dark matter of various spins (0, 1, $1/2$) in a framework of a consistent, renormalizable quantum field theory. Even if the ultimate theory of DM will prove to be non-minimal, it is reasonable to expect that the minimal models discussed here will capture its major low-energy properties. Our intention is to verify to what extent future e^+e^- colliders operating near $\sqrt{s} = 250\,\text{GeV}$: the Future Circular Collider (FCC-ee) [12–14], the Circular Electron Positron Collider (CEPC) [15] and the International Linear Collider (ILC) [16–18], could be useful for detecting DM in the process of mono-Z production, $e^+e^- \to Z + \cdots$. Our strategy is to impose existing constraints on simple models of pseudoscalar (pGDM), vector (VDM) and fermion (FDM) dark matter and determine regions of parameters in which the DM-production cross section at e^+e^- colliders is maximal. Then we compare the maximized predictions with the expected 95% CL cross-section limits at the ILC, assuming that it will provide a satisfactory estimate for the other colliders as well. That way we are trying to verify whether the future electron-positron colliders operating in the vicinity of $\sqrt{s} = 250\,\text{GeV}$ could be used to test theories of DM.

DM production at future e^+e^- colliders has already been discussed in the literature, see [19, 20]. However, our approach has another motivation, also the models adopted here are not the same. The goal of this project is different as well.

The paper is organized as follows: after the introduction in section 1, in the subsequent sections 2, 3 and 4 we describe the pseudo-Goldstone, vector and fermion dark matter models, respectively. Section 5 is devoted to the constraints on dark matter scenarios, that are adopted in the paper. In section 6 we calculate the cross section for the $e^+e^- \to Z + \cdots$ process and discuss subtleties of the mass degenerate case, $m_1 \simeq m_2$. The next section, section 7, is to review the expected sensitivity to this process at the ILC. Section 8 contains our numerical results with determination of regions in the parameter space that could be tested at the FCC-ee, CEPC and ILC. In the final section, section 9, we summarize our findings. In appendices we collect results concerning the Higgs boson decay widths and 2-point 1-loop scalar Green's functions.

2 Pseudo-Goldstone dark matter

In spite of the fact that the minimal model of scalar (spin zero) DM [21, 22] assumes merely an addition of a real scalar field odd under a $\mathbb{Z}_2$ symmetry, here we are going to consider a model (pGDM) that requires an extension by a complex scalar filed S. The model is in some sense very similar to vector and fermion dark matter models that will be discussed here as well, so it is worth to compare all of them. In order to stabilize a component of S we require an invariance under DM charge conjugation $C: \; S \to S^*$, which guarantees stability of the imaginary part of S, $A \equiv \text{Im}\, S/\sqrt{2}$. The real part, $\phi_S \equiv \text{Re}\, S/\sqrt{2}$, is going to develop a real vacuum expectation value (vev) $\langle \phi_S \rangle = \langle S \rangle = v_S/\sqrt{2}$.[1] Therefore, ϕ_S will mix with the neutral component of the SM Higgs doublet H, in exactly the same manner as it happens for the VDM or the FDM. In order to simplify the potential we impose in addition a $\mathbb{Z}_2$ symmetry $S \to -S$, which eliminates odd powers of S. Eventually, the scalar potential reads:

$$V = -\mu_H^2|H|^2 + \lambda_H|H|^4 - \mu_S^2|S|^2 + \lambda_S|S|^4 + \kappa|S|^2|H|^2 + \mu^2(S^2 + S^{*\,2}) \tag{2.1}$$

with μ^2 real, as implied by the C symmetry. Note that the μ^2 term breaks the U(1) explicitly, so the pseudo-Goldstone boson A is massive. In the limit of exact symmetry, A

---

[1] This is a choice that fixes the freedom (phase rotation of the complex scalar) of choosing a weak basis that could be adopted to formulate the model. The model is defined by symmetries imposed in this particular basis in which the scalar vacuum expectation value is real.

JHEP08(2020)052

would be just a genuine, massless Goldstone boson. Since the symmetry-breaking operator $\mu^2(S^2+S^{*\,2})$ is of dimension less that 4, its presence does not jeopardize renormalizability even if non-invariant higher dimension operators were not introduced, see for instance [23]. Note that dimension 3 terms are disallowed by the $\mathbb{Z}_2$ and gauge symmetries. In other words, we can limit ourself to dimension 2 U(1)-breaking terms preserving the renormalizability of the model. The freedom to introduce solely the soft breaking operators offers a very efficient and economical way to generate mass for the pseudo-scalar A without the necessity to introduce dimension 4 terms like S^4 or $|S|^2S^2$, and keeping the renormalizability of the model. It is also worth noticing that the $\mathbb{Z}_2$ symmetry $S\to -S$ is broken spontaneously by v_S and, therefore, ϕ_S, the real part of S, is not stable, making A the only DM candidate.

The scalar fields can be expanded around the corresponding generic vevs, v for H and v_S for S, as follows:

$$S=\frac{1}{\sqrt{2}}(v_S+iv_A+\phi_S+iA)\,,\quad H^0=\frac{1}{\sqrt{2}}(v+\phi_H+i\sigma_H)\quad \text{where } H=\begin{pmatrix}H^+\\ H^0\end{pmatrix}. \tag{2.2}$$

The global minimum of the potential with corresponding value of the potential and the scalar mass-squared matrix read:

$$v^2=\frac{4\lambda_S\mu_H^2-2\kappa(\mu_S^2-2\mu^2)}{4\lambda_H\lambda_S-\kappa^2}\,,\quad v_S^2=\frac{4\lambda_H(\mu_S^2-2\mu^2)-2\kappa\mu_H^2}{4\lambda_H\lambda_S-\kappa^2}\,,\quad v_A^2=0 \tag{2.3}$$

$$V_{\min}=\frac{-1}{4\lambda_H\lambda_S-\kappa^2}\left\{\lambda_H(\mu_S^2-2\mu^2)^2+\mu_H^2\left[\lambda_S\mu_H^2-\kappa(\mu_S^2-2\mu^2)\right]\right\}, \tag{2.4}$$

$$\mathcal{M}^2=\begin{pmatrix}2\lambda_Hv^2 & \kappa vv_S & 0\\ \kappa vv_S & 2\lambda_Sv_S^2 & 0\\ 0 & 0 & -4\mu^2\end{pmatrix} \tag{2.5}$$

in the basis (ϕ_H,ϕ_S,A). Note that the third spin-zero state A does not mix with the former ones.

Conditions necessary to guarantee the asymptotic positivity of the potential and the global minimum at $(v_H/\sqrt{2},v_S/\sqrt{2})$ with non-zero vevs will be discussed in section 5.5.

It is worth to notice that in the vector DM model considered in the following section, A becomes a genuine Goldstone boson ($\mu^2=0$) and disappears as a longitudinal component of the massive DM vector X.

There are two mass eigenstates, h_1 and h_2, in this model. The mass matrix (2.5) can be diagonalized by the orthogonal rotation matrix $\mathcal{R}^{-1}$ acting on the space spanned by the two CP-even scalars ϕ_H and ϕ_S:

$$\begin{pmatrix}h_1\\ h_2\end{pmatrix}=\mathcal{R}^{-1}\begin{pmatrix}\phi_H\\ \phi_S\end{pmatrix}=\begin{pmatrix}\cos\alpha & \sin\alpha\\ -\sin\alpha & \cos\alpha\end{pmatrix}\begin{pmatrix}\phi_H\\ \phi_S\end{pmatrix}, \tag{2.6}$$

with

$$\tan 2\alpha=\frac{2\mathcal{M}_{12}^2}{\mathcal{M}_{11}^2-\mathcal{M}_{22}^2}\,. \tag{2.7}$$

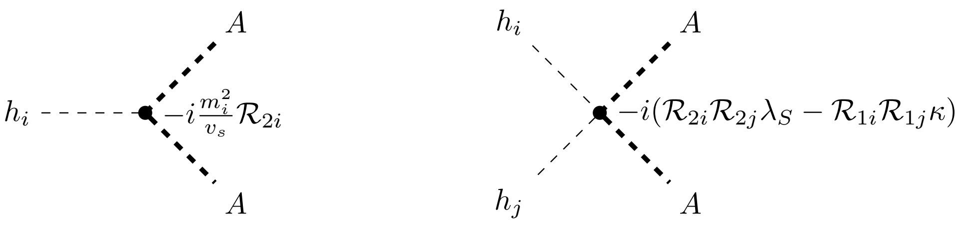

Figure 1. Vertices relevant for the pGDM model.

We assume hereafter that h_1 is the 125.09 GeV boson observed at the LHC. Moreover, since $\sin\alpha$ appears in calculations of sections 5 and 6 in the second power, we will assume without losing generality that the sign of κ is chosen in such a way that $\sin\alpha > 0$.

We choose as independent parameters of the model the set: v_S, $\sin\alpha$, m_2 and $m_{\rm DM} = m_A$. Together with $v = 246.22\,\text{GeV}$ and $m_1 = 125.09\,\text{GeV}$ this set is sufficient to determine all the 6 parameters of the potential; relevant relations will be presented in section 5.5. As it will be seen later, scalar potentials in other theories discussed in this work could be also parametrized in terms of the same parameters, allowing for meaningful comparison between the models.[2]

Vertices relevant for the calculation of annihilation cross section in the pGDM model have been collected in figure 1.

Similar models have been considered in a more general context including a possibility of fast first-order phase transition in [24–26]. However, those models have different phenomenology, as the pGDM model possesses the unique and attractive feature of natural suppression of DM scattering against nuclei. This property of the pGDM is a consequence of the particular way of soft breaking of the $\mathrm{U}(1)_X$ by the terms that are quadratic in S, see [27]. This aspect will be particularly relevant in section 5.3.

3 Vector dark matter

The next model that we want to compare with the pGDM is the popular vector DM (VDM) model [28–33] that is an extension of the SM by an additional $\mathrm{U}(1)_X$ gauge symmetry and a complex scalar field S, whose vev generates a mass for the corresponding gauge field. The quantum numbers of the scalar field are

$$S = (0, \mathbf{1}, \mathbf{1}, 1) \quad \text{under} \quad \mathrm{U}(1)_Y \times \mathrm{SU}(2)_L \times \mathrm{SU}(3)_c \times \mathrm{U}(1)_X . \tag{3.1}$$

None of the SM fields are charged under the extra gauge group. In order to ensure stability of the new vector boson a $\mathbb{Z}_2$ symmetry is assumed to forbid U(1)-kinetic mixing between $\mathrm{U}(1)_X$ and $\mathrm{U}(1)_Y$. The extra gauge boson X and the scalar field S transform under the $\mathbb{Z}_2$ as follows

$$X \to -X\,, \qquad S \to S^*\,. \tag{3.2}$$

All other fields are neutral under the $\mathbb{Z}_2$.

---

[2] Here, the DM mass m_A is also a parameter of the potential. In the remaining models discussed in this paper, DM masses will be independent parameters.

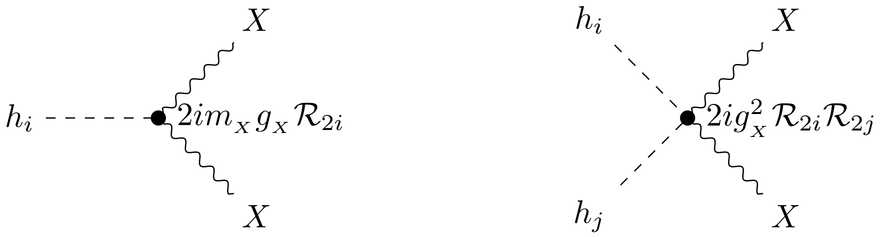

Figure 2. The vertices relevant for the VDM model.

The vector bosons' masses are given by:

$$m_W = \frac{1}{2}gv\,, \qquad m_Z = \frac{1}{2}\sqrt{g^2+g'^2}\,v \qquad \text{and} \qquad m_X = g_X v_S, \tag{3.3}$$

where g and g' are the SU(2) and U(1) gauge couplings, while, as in the previous model, v and v_S are the vevs of H and S, respectively: $(\langle H\rangle, \langle S\rangle) = \frac{1}{\sqrt{2}}(v, v_S)$.[3] The scalar potential for this model is given by

$$V = -\mu_H^2|H|^2 + \lambda_H|H|^4 - \mu_S^2|S|^2 + \lambda_S|S|^4 + \kappa|S|^2|H|^2. \tag{3.4}$$

It is easy to find solutions of the potential minimization conditions for the scalar fields:

$$v^2 = \frac{4\lambda_S\mu_H^2 - 2\kappa\mu_S^2}{4\lambda_H\lambda_S - \kappa^2}\,, \qquad v_S^2 = \frac{4\lambda_H\mu_S^2 - 2\kappa\mu_H^2}{4\lambda_H\lambda_S - \kappa^2}\,. \tag{3.5}$$

Both scalar fields can be expanded around the corresponding vevs as follows

$$S = \frac{1}{\sqrt{2}}(v_S + \phi_S + i\sigma_S)\,, \quad H^0 = \frac{1}{\sqrt{2}}(v + \phi_H + i\sigma_H) \quad \text{where} \quad H = \begin{pmatrix} H^+ \\ H^0 \end{pmatrix}. \tag{3.6}$$

The mass-squared matrix $\mathcal{M}^2$ for the fluctuations (ϕ_H, ϕ_S) is identical as the 2×2 block of the mass matrix for the pGDM model (2.5), so that the diagonalization (2.6) and relation (2.7) remain applicable.

Conditions for existence of non-zero vevs, globality of the minimum and asymptotic positivity of the potential will be discussed in section 5.5. The input parameters adopted here are: v_S, $\sin\alpha$, m_2 and $m_{\rm DM} = m_X$.

Vertices relevant for the calculation of annihilation cross section in the VDM model have been collected in figure 2. It is interesting to notice similarity between the VDM and the pGDM. In the latter one the $U(1)_X$ (that is a gauge symmetry of the VDM) is explicitly (but softly) broken. The corresponding pseudo-Goldstone boson A in the pGDM model remains in the spectrum of scalars, while in the VDM this degree of freedom disappears as a longitudinal component of the massive vector X.

4 Fermion dark matter

In the case of minimal fermion DM, the gauge group remains the standard one, i.e. $U(1)_Y \times SU(2)_L \times SU(3)_c$. This model can be treated as a special case of the singlet-singlet model

---

[3] $\langle H\rangle$ and $\langle S\rangle$ could be chosen to be real and non-negative without losing generality.

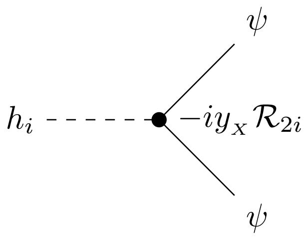

Figure 3. The vertex relevant for the FDM model.

discussed in [34]. The DM candidate χ (left-handed Dirac fermion) is introduced together with a real scalar S that is necessary to mediate DM interaction with the SM.

The extra states are charged under $\mathbb{Z}_4$: $S \to -S$ while $\chi \to i\chi$. The resulting symmetric Lagrangian reads:

$$\mathcal{L} = \mathcal{L}_{\rm SM} + i\bar\chi\not\partial\chi + \frac{1}{2}\partial^\mu S\,\partial_\mu S - \frac{y_\chi}{2}(\bar\chi^c\chi + \bar\chi\chi^c)S - V(H,S)\,, \tag{4.1}$$

$$V(H,S) = -\mu_H^2|H|^2 + \lambda_H|H|^4 - \frac{\mu_S^2}{2}S^2 + \frac{\lambda_S}{4}S^4 + \frac{\kappa}{2}|H|^2S^2\,, \tag{4.2}$$

where $\chi^c \equiv -i\gamma_2\chi^*$. Note that the above potential is the same as in the VDM case (see (3.4)), up to normalization of the singlet mass and its couplings. The positivity conditions of the potential remain, of course, the same for this model as for the previous two since all the potentials have the same asymptotic behaviour.

We parametrize fluctuations of scalar fields as follows:

$$S = v_S + \phi_S\,, \qquad H^0 = \frac{1}{\sqrt{2}}(v + \phi_H + i\sigma_H) \qquad \text{where} \qquad H = \begin{pmatrix} H^+ \\ H^0 \end{pmatrix}, \tag{4.3}$$

with v and v_S being the vevs of the neutral component of the doublet H and the singlet S, respectively, determined by (3.5).

After SSB, relevant parts of the Lagrangian take the following form:

$$i\bar\chi\not\partial\chi + \frac{1}{2}\partial^\mu S\,\partial_\mu S - \frac{y_\chi}{2}(\bar\chi^c\chi + \bar\chi\chi^c)S \to \frac{i}{2}\bar\psi\not\partial\psi + \frac{1}{2}\partial^\mu\phi_S\,\partial_\mu\phi_S - \frac{y_\chi v_S}{2}\bar\psi\psi - \frac{y_\chi}{2}\bar\psi\psi\phi_S \tag{4.4}$$

where $\psi = \psi^c \equiv \chi + \chi^c$ is a Majorana mass eigenstate with $m_\psi = y_\chi v_S$.

Here, as in the models discussed earlier, there are two physical (mass eigenstates) scalar degrees of freedom, h_1 and h_2, that are linear combinations of ϕ_H and ϕ_S. Note that because of appropriate normalization of terms involving S in the potential (4.2) the mass matrix and its diagonalization remain the same as in the other models. It is convenient to use the analogous input parameters to discuss this model: v_S, $\sin\alpha$, m_2, and $m_{\rm DM} = m_\psi$.

Positivity and minimization conditions for this model will be discussed in section 5.5.

Figure 3 presents the vertex relevant for the calculation of annihilation cross section in the FDM model.

5 Astrophysical and other constraints

Hereafter we are going to allow for resonant DM annihilation process, so we will adopt the Breit-Wigner propagators for mediating particles, i.e. the Higgs bosons $h_{1,2}$. $\Gamma_{1,2}$ will denote the total width of $h_{1,2}$, respectively.

5.1 Dark matter abundance

The thermally averaged cross section for DM annihilation into a SM fermion-anti-fermion pair, $\sigma(\mathrm{DM\ DM} \to \bar{f}f)$, reads:[4]

$$\begin{aligned}\langle\sigma v\rangle = \frac{n_c}{3}\frac{m_{\mathrm{DM}} m_f^2}{\pi}\cdot\mathcal{X}\cdot&\frac{\left(m_{\mathrm{DM}}^2 - m_f^2\right)^{3/2}}{\left[(4m_{\mathrm{DM}}^2-m_1^2)^2+m_1^2\Gamma_1^2\right]\left[(4m_{\mathrm{DM}}^2-m_2^2)^2+m_2^2\Gamma_2^2\right]}\cdot\\ &\times\begin{cases}12+\mathcal{O}\left[\left(\frac{m_{\mathrm{DM}}}{T}\right)^{-1}\right] & \text{(pGDM)}\\ 1+\mathcal{O}\left[\left(\frac{m_{\mathrm{DM}}}{T}\right)^{-1}\right] & \text{(VDM)}\\ \frac{9}{4}\left(\frac{m_{\mathrm{DM}}}{T}\right)^{-1}+\mathcal{O}\left[\left(\frac{m_{\mathrm{DM}}}{T}\right)^{-2}\right] & \text{(FDM)}\end{cases},\end{aligned} \tag{5.1}$$

with $n_c = 1(3)$ for f being lepton (quark) and the variable $\mathcal{X}$ defined[5] as

$$\mathcal{X} \equiv (\sin\alpha\cos\alpha)^2\frac{\left[(m_1^2-m_2^2)^2+(m_1\Gamma_1-m_2\Gamma_2)^2\right]}{v^2 v_S^2}. \tag{5.2}$$

The DM abundance observed by the Planck Collaboration [10],

$$\left(\Omega h^2\right)_{\mathrm{DM}}^{\mathrm{obs}} = 0.1186 \pm 0.002\,, \tag{5.3}$$

constraints the annihilation cross section at the freeze-out temperature by

$$\langle\sigma v\rangle\Big|_{\text{freeze out}} = (n+1)\cdot 2.2\cdot 10^{-26}\ \mathrm{cm^3\,s^{-1}} = (n+1)\cdot 1.9\cdot 10^{-9}\,\mathrm{GeV}^{-2}\,, \tag{5.4}$$

what corresponds to the current value of annihilation cross section equal to

$$\langle\sigma v\rangle\Big|_{\text{now}} = (T_0/T_f)^n\cdot\langle\sigma v\rangle\Big|_{\text{freeze out}} = (T_0/T_f)^n\cdot(n+1)\cdot 1.9\cdot 10^{-9}\,\mathrm{GeV}^{-2}\,, \tag{5.5}$$

where T_0 is the present CMB temperature while $T_f \sim m_{\mathrm{DM}}/25$ is temperature at the moment of freeze out. Value of n is 0 for the bosonic models (pGDM, VDM) and 1 for the FDM.

Hence, keeping only the leading ($b\bar{b}$) contribution in eq. (5.1), we obtain the following constraint

$$\begin{aligned}\mathcal{X} \simeq &\frac{\left[(m_1^2-4m_{\mathrm{DM}}^2)^2+m_1^2\Gamma_1^2\right]\left[(m_2^2-4m_{\mathrm{DM}}^2)^2+m_2^2\Gamma_2^2\right]}{m_{\mathrm{DM}}(m_{\mathrm{DM}}^2-m_b^2)^{3/2}}\times\\ &\times 3.5\cdot 10^{-10}\,\mathrm{GeV}^{-4}\cdot\begin{cases}1/12 & \text{(pGDM)}\\ 1 & \text{(VDM)}\\ 22 & \text{(FDM)}\end{cases}.\end{aligned} \tag{5.6}$$

---

[4] Other final states are not accessible kinematically for mass ranges considered here.

[5] Note that at the tree level $\mathcal{X}$ reduces to κ^2.

5.2 Dark matter indirect detection

Since we fix the DM abundance to its observed value (5.3), the present annihilation cross section is also fixed by (5.5), so that it remains to be a function of $m_{\rm DM}$ only. Therefore, the limit on the present annihilation cross section, for instance from Fermi-LAT [35], implies a lower limit on DM mass. For the bosonic models (pGDM, VDM), adopting data for the $b\bar{b}$ final state, one obtains $m_{\rm DM} \gtrsim 20\,{\rm GeV}$. Hereafter, we will consider this region only. In the case of the FDM, the extra suppression by T_0/T_f implies that the cross section is by a factor of 10^{-11}–10^{-13} smaller than for the bosonic models and, therefore, there is no constraint on m_ψ.

5.3 Dark matter direct detection

The DM direct detection (DD) experiments impose severe constraints on the parameter space of DM models. In the models discussed here the spin-independent cross sections for the DM-nucleon scattering are given by

$$\sigma_{\rm SI} \simeq \frac{\mu^2 f_N^2}{\pi} \cdot \mathcal{X} \cdot \frac{m_{\rm DM}^2 m_N^2}{m_1^4 m_2^4} \begin{cases} \left[\frac{\mathcal{A}}{64\pi^2 v v_S^2}\right]^2 & ({\rm pGDM}) \\ 1 & ({\rm VDM}), ({\rm FDM}) \,, \end{cases} \tag{5.7}$$

where m_N denotes nucleon mass and μ is the reduced mass for the DM-nucleon system while for the form factor we have adopted $f_N \simeq 0.3\,{\rm GeV}$. Widths and momentum transfer in the denominator have been neglected as much smaller than masses. It turns out that in the pGDM model the cross section vanishes [27, 36, 37] in the limit of zero momentum transfer, so 1-loop calculations are needed. The 1-loop results are encoded above through the factor containing $\mathcal{A}$, defined according to [36][6] as

$$\begin{aligned} \mathcal{A} = a_1 \cdot C(0, m_{\rm DM}; m_1, m_2, m_{\rm DM}) + \\ a_2 \cdot D(0, 0, m_{\rm DM}; m_1, m_1, m_2, m_{\rm DM}) + \\ a_3 \cdot D(0, 0, m_{\rm DM}; m_1, m_2, m_2, m_{\rm DM}) \end{aligned} \tag{5.8}$$

with

$$\begin{aligned} a_1 &= 4(m_1^2 \sin^2\alpha + m_2^2 \cos^2\alpha) \left[2v(m_1^2 \sin^2\alpha + m_2^2\cos^2\alpha) - (m_1^2 - m_2^2) v_S \sin 2\alpha\right] \,, \\ a_2 &= -2m_1^4 \sin\alpha \left[(m_1^2 + 5m_2^2) v_S \cos\alpha - (m_1^2 - m_2^2)(v_S \cos 3\alpha + 4v\sin^3\alpha)\right] \,, \\ a_3 &= 2m_2^4 \cos\alpha \left[(5m_1^2 + m_2^2) v_S \sin\alpha - (m_1^2 - m_2^2)(v_S \sin 3\alpha + 4v\cos^3\alpha)\right] \,, \end{aligned} \tag{5.9}$$

where the functions C and D are defined in appendix B. In eq. (5.9), the sign of $\sin\alpha$ is relevant, what seems to contradict our statement that chosing $\sin\alpha > 0$ does not spoil generality of our considerations. However, the only place where we use results of eq. (5.7) for the pGDM is the comparison in figure 4. Regardless of the sign of $\sin\alpha$, the conclusion that $\mathcal{X}({\rm DD})$ is orders of magnitude larger than $\mathcal{X}(\Omega_0^{\rm DM})$ remains true, and hence, we do not have to consider the $\sin\alpha < 0$ case separately.

---

[6] In appendix B of [36], the factor $1/(2\pi)^4$ in definitions of loop integrals should be replaced by $1/(i\pi^2)$. Nonetheless, all results in the main text of the paper are correct.

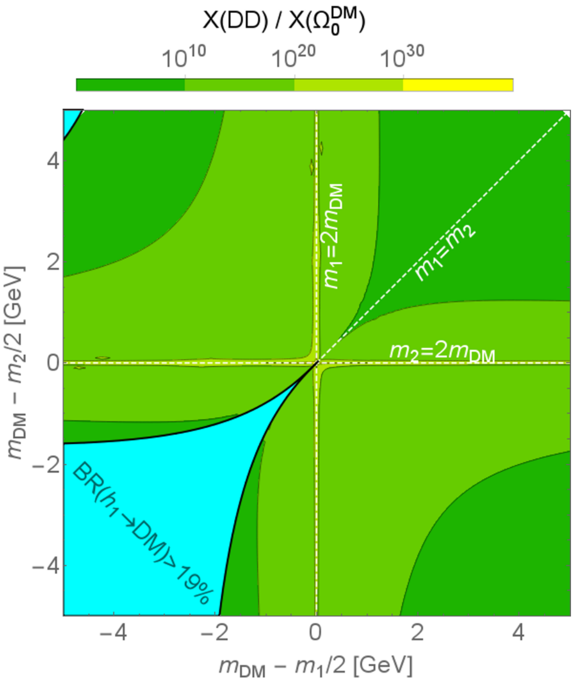

Figure 4. Comparison between the DD upper bound for the value of $\mathcal{X}$ (denoted by $\mathcal{X}$(DD), see eq. (5.11)) and the value providing correct relic density (denoted by $\mathcal{X}(\Omega_0^{\rm DM})$, see eq. (5.6)), in the case of the pGDM. Since the upper bound is always higher than the required value, the DD constraint does not affect the range of (m_2,$m_{\rm DM}$) in the case of this model.

For practical purposes, the XENON1T limit [38] for $m_{\rm DM} \gtrsim 40\,$GeV can be parametrized as follows

$$\frac{\sigma_{\rm SI}^{\rm max}}{1\ {\rm cm}^2} \simeq \frac{m_{\rm DM}}{1\,{\rm GeV}}\cdot 10^{-48.05}\,. \tag{5.10}$$

Hence, $\mathcal{X}$ is constrained from above by DD limit:

$$\begin{aligned}\mathcal{X} &\lesssim \frac{m_1^4 m_2^4}{m_{\rm DM} m_N^2 f_N^2}\frac{\pi}{\mu^2}\frac{1\ {\rm cm}^2}{1\,{\rm GeV}}\cdot 10^{-48.05}\begin{cases}\left[\frac{\mathcal{A}}{64\pi^2 v v_S^2}\right]^{-2} & ({\rm pGDM})\\ 1 & ({\rm VDM}),({\rm FDM})\end{cases},\\ &\simeq \frac{m_2^4}{m_{\rm DM}}\cdot 2.5\cdot 10^{-11}\,{\rm GeV}^{-3}\begin{cases}\left[\frac{\mathcal{A}}{64\pi^2 v v_S^2}\right]^{-2} & ({\rm pGDM})\\ 1 & ({\rm VDM}),({\rm FDM})\end{cases}.\end{aligned} \tag{5.11}$$

It turns out that in the considered range of parameters, in the case of the pGDM, the DD upper bound on the value of $\mathcal{X}$ is always higher than the value corresponding to the correct relic density, see figure 4. Therefore, in the case of the pGDM, the DD constraint does not limit the range of $(m_2, m_{\rm DM})$.

5.4 Collider constraints

The mixing angle α is constrained from the measurement of the SM signal strength $\mu_{\rm LHC}$. The latest LHC bound is $\mu_{\rm LHC} = 1.09 \pm 0.11$ which amounts to $\sin^2\alpha < 0.13$ at the 2σ CL [39]. Hereafter we will adopt a bit stronger limit $\sin\alpha < 0.30$.

When the DM mass is smaller than half of the SM-like Higgs boson h_1, $m_{\rm DM} < m_1/2$, the Higgs invisible decay provides another constraint on DM scenarios. In the models discussed here, the width for invisible decays are as follows

$$\begin{aligned}\Gamma_{h_i\to{\rm DM}} = \frac{\mathcal{R}_{2i}^2}{v_S^2}\cdot\frac{m_i^3}{32\pi}\sqrt{1-\frac{4m_{\rm DM}^2}{m_i^2}}\times \\ \times\begin{cases}1 & \text{(pGDM)}\\ 1-4\frac{m_{\rm DM}^2}{m_i^2}+12\left(\frac{m_{\rm DM}^2}{m_i^2}\right)^2 & \text{(VDM)}\\ 2\frac{m_{\rm DM}^2}{m_i^2}\left(1-4\frac{m_{\rm DM}^2}{m_i^2}\right) & \text{(FDM)}\end{cases}\end{aligned} \quad . \tag{5.12}$$

Current LHC measurements [40] provides the following limit on the invisible branchig ratio:

$$\mathrm{BR}(h_1\to \mathrm{inv}) < 19\% \tag{5.13}$$

at the 95% CL.

5.5 Theoretical constraints

In order to ensure that the leading order calculations adopted here are meaningful, we impose the following perturbativity conditions on the $\mathrm{U}(1)_X$ gauge coupling in the VDM model and the Yukawa coupling in the FDM model: $g_X < 4\pi$ and $y_X < 4\pi$. Both of them correspond to $v_S > \frac{m_{\rm DM}}{4\pi}$. In the pGDM model, the AAh_i coupling is proportional to m_i^2/v_S (cf. figure 1), therefore we also require $m_i/v_S < 4\pi$ $(i = 1, 2)$. It is interesting to note that there exist regions (e.g. $m_2 \sim m_1$) in the parameter space where the proper abundance of DM requires small v_S. In these regions some quartic couplings might be too large (non-perturbative), since $\lambda_S \propto m_i^2/v_S^2$ and $\kappa \propto (m_1^2 - m_2^2)/(vv_S)$, see figure 11. Therefore we also impose the conditions: $\lambda_S, |\kappa| < 4\pi$. Summing up, the conditions adopted here in order to ensure perturbativity within considered models are

$$\underbrace{\frac{m_{\rm DM}}{v_S} < 4\pi}_{\text{for VDM and FDM}}\quad,\qquad \underbrace{\frac{m_i}{v_S} < 4\pi}_{\text{for pGDM}}\,,\qquad \lambda_S < 4\pi\,,\qquad |\kappa| < 4\pi\,. \tag{5.14}$$

Let us now consider conditions for stability of the vacuum state. Scalar potentials of the models read (see eqs. (2.1), (3.4) and (4.2)):

$$\begin{aligned}V_{\rm pGDM}(H,S) &= -\mu_H^2|H|^2+\lambda_H|H|^4-\mu_S^2|S|^2+\lambda_S|S|^4+\kappa|H|^2|S|^2+ \\ &\quad +\mu^2(S^2+S^{*2})\,,\end{aligned} \tag{5.15}$$

$$V_{\rm VDM}(H,S) = -\mu_H^2|H|^2+\lambda_H|H|^4-\mu_S^2|S|^2+\lambda_S|S|^4+\kappa|H|^2|S|^2\,, \tag{5.16}$$

$$V_{\rm FDM}(H,S) = -\mu_H^2|H|^2+\lambda_H|H|^4-\frac{\mu_S^2}{2}S^2+\frac{\lambda_S}{4}S^4+\frac{\kappa}{2}|H|^2S^2\,. \tag{5.17}$$

To ensure asymptotic positivity of all the potentials, the following conditions must be satisfied:

$$\lambda_H > 0\,,\qquad \lambda_S > 0\,,\qquad \kappa > -2\sqrt{\lambda_H\lambda_S}\,. \tag{5.18}$$

Vacuum expectation values of the scalar fields H, S are denoted as follows

$$\langle H\rangle = v/\sqrt{2}\,, \qquad \langle S\rangle = v_S/\sqrt{2} \qquad \text{(pGDM, VDM)}\,, \tag{5.19}$$

$$\langle H\rangle = v/\sqrt{2}\,, \qquad \langle S\rangle = v_S \qquad \text{(FDM)}\,. \tag{5.20}$$

In each case, $v, v_S \neq 0$ must minimize the value of the potential. The corresponding point in the (H,S) space is a critical one if and only if

$$v^2 = 2\,\frac{2\lambda_S\mu_H^2 - \kappa(\mu_S^2 - 2\mu^2)}{4\lambda_H\lambda_S - \kappa^2}\,, \qquad v_S^2 = 2\,\frac{2\lambda_H(\mu_S^2 - 2\mu^2) - \kappa\mu_H^2}{4\lambda_H\lambda_S - \kappa^2} \tag{5.21}$$

in the case of the pGDM and

$$v^2 = 2\,\frac{2\lambda_S\mu_H^2 - \kappa\mu_S^2}{4\lambda_H\lambda_S - \kappa^2}\,, \qquad v_S^2 = 2\,\frac{2\lambda_H\mu_S^2 - \kappa\mu_H^2}{4\lambda_H\lambda_S - \kappa^2} \tag{5.22}$$

in the case of the VDM and the FDM.

To ensure that the critical point is a strict minimum, we demand the second derivative of the potential to be positive definite, therefore

$$0 < \partial^2_{H,H}V = 4\lambda_H v^2\,, \tag{5.23}$$

$$0 < \det(D^2V) = 4v^2v_S^2(4\lambda_H\lambda_S - \kappa^2)\cdot\begin{cases}1 & \text{(pGDM, VDM)}\\ 1/2 & \text{(FDM)}\end{cases}\,. \tag{5.24}$$

Hence, assuming v^2, v_S^2 and λ_H are positive, the following condition must hold

$$4\lambda_H\lambda_S - \kappa^2 > 0\,. \tag{5.25}$$

Positivity of the vevs squared requires (cf. eqs. (5.21) and (5.22))

$$2\lambda_S\mu_H^2 - \kappa(\mu_S^2 - 2\mu^2) > 0\,, \qquad 2\lambda_H(\mu_S^2 - 2\mu^2) - \kappa\mu_H^2 > 0 \tag{5.26}$$

in the case of the pGDM and

$$2\lambda_S\mu_H^2 - \kappa\mu_S^2 > 0\,, \qquad 2\lambda_H\mu_S^2 - \kappa\mu_H^2 > 0 \tag{5.27}$$

in the case of the VDM and the FDM.

Let us check when the points given by eqs. (5.21) and (5.22) are global minima. In the case of the pGDM, due to the presence of the $\mu^2(S^2 + S^{*2})$ term, in principle the phase of the vacuum expectation value of S could be relevant. Hence, let us assume that $\langle S\rangle = (v_S + iv_A)/\sqrt{2}$. Now, we have to minimize the potential with respect to v, v_S and

v_A. There are six critical points of the potential, namely

$$(v^2\,,\,v_S^2\,,\,v_A^2) = (0\,,\,0\,,\,0)\,, \qquad V = 0\,, \tag{5.28}$$

$$(v^2\,,\,v_S^2\,,\,v_A^2) = \left(\frac{\mu_H^2}{2\lambda_H}\,,\,0\,,\,0\right)\,, \qquad V = -\frac{\mu_H^4}{4\lambda_H}\,, \tag{5.29}$$

$$(v^2\,,\,v_S^2\,,\,v_A^2) = \left(0\,,\,\frac{\mu_S^2 - 2\mu^2}{2\lambda_S}\,,\,0\right)\,, \qquad V = -\frac{(\mu_S^2 - 2\mu^2)^2}{4\lambda_S}\,, \tag{5.30}$$

$$(v^2\,,\,v_S^2\,,\,v_A^2) = \left(0\,,\,0\,,\,\frac{\mu_S^2 + 2\mu^2}{2\lambda_S}\right)\,, \qquad V = -\frac{(\mu_S^2 + 2\mu^2)^2}{4\lambda_S}\,, \tag{5.31}$$

$$\begin{aligned}(v^2\,,\,v_S^2\,,\,v_A^2) &= \left(2\,\frac{2\lambda_S\mu_H^2 - \kappa(\mu_S^2 + 2\mu^2)}{4\lambda_H\lambda_S - \kappa^2}\,,\,0\,,\,2\,\frac{2\lambda_H(\mu_S^2 + 2\mu^2) - \kappa\mu_H^2}{4\lambda_H\lambda_S - \kappa^2}\right)\,,\\ V &= -\frac{\lambda_H(\mu_S^2 + 2\mu^2)^2 + \lambda_S\mu_H^4 - \kappa\mu_H^2(\mu_S^2 + 2\mu^2)}{4\lambda_H\lambda_S - \kappa^2}\,,\end{aligned} \tag{5.32}$$

$$\begin{aligned}(v^2\,,\,v_S^2\,,\,v_A^2) &= \left(2\,\frac{2\lambda_S\mu_H^2 - \kappa(\mu_S^2 - 2\mu^2)}{4\lambda_H\lambda_S - \kappa^2}\,,\,2\,\frac{2\lambda_H(\mu_S^2 - 2\mu^2) - \kappa\mu_H^2}{4\lambda_H\lambda_S - \kappa^2}\,,\,0\right)\,,\\ V &= -\frac{\lambda_H(\mu_S^2 - 2\mu^2)^2 + \lambda_S\mu_H^4 - \kappa\mu_H^2(\mu_S^2 - 2\mu^2)}{4\lambda_H\lambda_S - \kappa^2}\,.\end{aligned} \tag{5.33}$$

Assuming the asymptotic positivity conditions (5.18), the strict-minimum condition (5.25) and positivity of $m_{\mathrm{DM}}^2 = -4\mu^2$, minimum (5.33) is always smaller than (5.29) and (5.30). To ensure that minimum (5.33) is smaller than (5.32), the following additional condition must hold:

$$2\lambda_H\mu_S^2 - \kappa\mu_H^2 > 0\,. \tag{5.34}$$

Value of (5.31) is obviously greater than (5.30) and, therefore, greater than (5.33) if

$$\mu_S^2 > 0\,. \tag{5.35}$$

Both of these conditions are checked for considered region of parameter space at the end of this subsection.

In the case of the VDM and the FDM, we can assume that $\langle S\rangle$ is purely real without losing generality. Therefore, V is minimized with respect to v and v_S. The critical points are

$$(v^2\,,\,v_S^2) = (0\,,\,0)\,, \qquad V = 0\,, \tag{5.36}$$

$$(v^2\,,\,v_S^2) = \left(\frac{\mu_H^2}{2\lambda_H}\,,\,0\right)\,, \qquad V = -\frac{\mu_H^4}{4\lambda_H}\,, \tag{5.37}$$

$$(v^2\,,\,v_S^2) = \left(0\,,\,\frac{\mu_S^2}{2\lambda_S}\right)\,, \qquad V = -\frac{\mu_S^4}{4\lambda_S}\,, \tag{5.38}$$

$$\begin{aligned}(v^2\,,\,v_S^2) &= \left(2\,\frac{2\lambda_S\mu_H^2 - \kappa\mu_S^2}{4\lambda_H\lambda_S - \kappa^2}\,,\,2\,\frac{2\lambda_H\mu_S^2 - \kappa\mu_H^2}{4\lambda_H\lambda_S - \kappa^2}\right)\,,\\ V &= -\frac{\lambda_H\mu_S^4 + \lambda_S\mu_H^4 - \kappa\mu_H^2\mu_S^2}{4\lambda_H\lambda_S - \kappa^2}\,.\end{aligned} \tag{5.39}$$

This time, the asymptotic positivity conditions (5.18) and the strict-minimum condition (5.25) are enough to keep (5.39) a global minimum.

We can express parameters of the potential in terms of the input parameters: m_1, m_2, v, v_S, $m_{\rm DM}$ and $\sin\alpha$ as follows:

$$\mu^2 = -\frac{1}{4}m_{\rm DM}^2 \text{ (pGDM case only)}\,, \qquad \kappa = \frac{(m_1^2 - m_2^2)\sin 2\alpha}{2vv_S}\,, \tag{5.40}$$

$$\mu_H^2 = \frac{1}{2}m_1^2\cos^2\alpha + \frac{1}{2}m_2^2\sin^2\alpha + \frac{1}{4}\frac{v_S}{v}(m_1^2 - m_2^2)\sin 2\alpha\,, \tag{5.41}$$

$$\begin{aligned}\mu_S^2 = {}& \frac{1}{2}m_1^2\sin^2\alpha + \frac{1}{2}m_2^2\cos^2\alpha + \frac{1}{4}\frac{v}{v_S}(m_1^2 - m_2^2)\sin 2\alpha + \\ & - \begin{cases} \frac{1}{2}m_{\rm DM}^2 & \text{(pGDM)} \\ 0 & \text{(VDM, FDM)} \end{cases}\,,\end{aligned} \tag{5.42}$$

$$\lambda_H = \frac{m_1^2\cos^2\alpha + m_2^2\sin^2\alpha}{2v^2}\,, \qquad \lambda_S = \frac{m_1^2\sin^2\alpha + m_2^2\cos^2\alpha}{2v_S^2}\,. \tag{5.43}$$

It appears that the stability and positivity conditions (5.18), (5.25) and (5.26) expressed in terms of the input parameters are automatically satisfied:

$$0 < \lambda_H \qquad \Leftrightarrow \qquad 0 < \frac{m_1^2\cos^2\alpha + m_2^2\sin^2\alpha}{2v^2}\,, \tag{5.44}$$

$$0 < \lambda_S \qquad \Leftrightarrow \qquad 0 < \frac{m_1^2\sin^2\alpha + m_2^2\cos^2\alpha}{2v_S^2}\,, \tag{5.45}$$

$$0 < 4\lambda_H\lambda_S - \kappa^2 \qquad \Leftrightarrow \qquad 0 < \frac{m_1^2 m_2^2}{v^2 v_S^2}\,, \tag{5.46}$$

$$0 < \begin{cases} 2\lambda_S\mu_H^2 - \kappa(\mu_S^2 - 2\mu^2) & \text{(pGDM)} \\ 2\lambda_S\mu_H^2 - \kappa\mu_S^2 & \text{(VDM, FDM)} \end{cases} \qquad \Leftrightarrow \qquad 0 < \frac{m_1^2 m_2^2}{2v_S^2}\,, \tag{5.47}$$

$$0 < \begin{cases} 2\lambda_H(\mu_S^2 - 2\mu^2) - \kappa\mu_H^2 & \text{(pGDM)} \\ 2\lambda_H\mu_S^2 - \kappa\mu_H^2 & \text{(VDM, FDM)} \end{cases} \qquad \Leftrightarrow \qquad 0 < \frac{m_1^2 m_2^2}{2v^2}\,. \tag{5.48}$$

In fact, our choice of the input set implicitly assumes that coefficients of V are such that $v^2, v_S^2, m_1^2, m_2^2 > 0$.

The global-minimum conditions (5.34) and (5.35) for the case of the pGDM are expressed in terms of the input parameters as follows:

$$0 < (2\lambda_H\mu_S^2 - \kappa\mu_H^2) \quad \Leftrightarrow \quad 0 < \frac{2m_1^2 m_2^2 - (m_1^2 + m_2^2)m_{\rm DM}^2 + (-m_1^2 + m_2^2)m_A^2\cos(2\alpha)}{4v^2}\,, \tag{5.49}$$

$$0 < \mu_S^2 \quad \Leftrightarrow \quad 0 < \frac{1}{2}m_1^2\sin^2\alpha + \frac{1}{2}m_2^2\cos^2\alpha + \frac{1}{4}\frac{v}{v_S}(m_1^2 - m_2^2)\sin 2\alpha - \frac{1}{2}m_{\rm DM}^2\,. \tag{5.50}$$

It can be numerically shown (see figure 5) that in the considered range of masses these conditions are always satisfied.

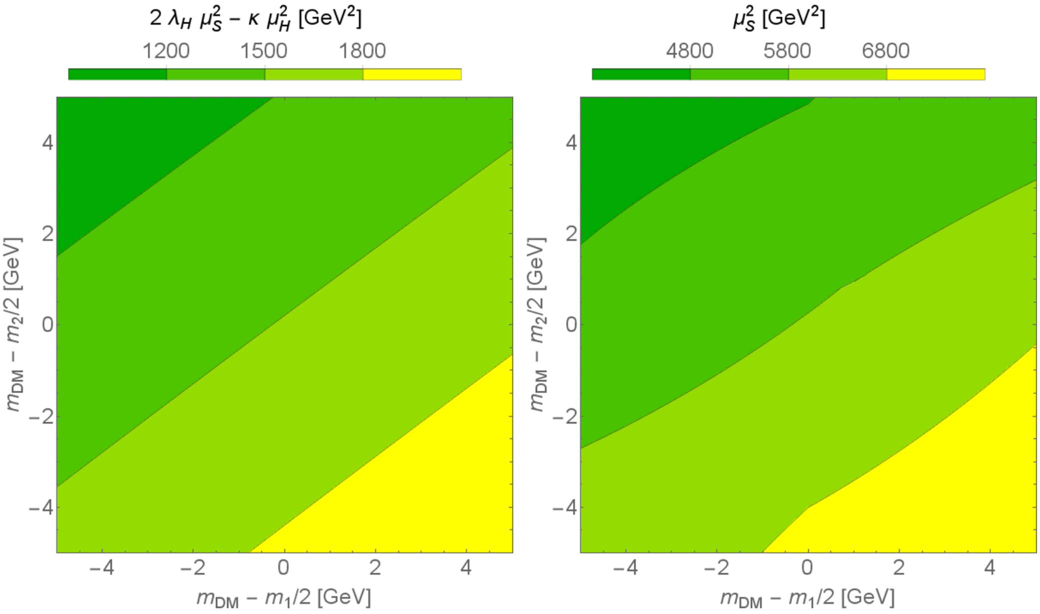

Figure 5. Numerical test of the conditions (5.49) (left pannel) and (5.50) (right pannel) for globalness of the minimum of the scalar potential in the pGDM model. If the plotted values are positive, the conditions are satisfied. Value of $\sin\alpha$ has been assumed to be 0.3. Value of v_S has been calculated from eq. (5.6).

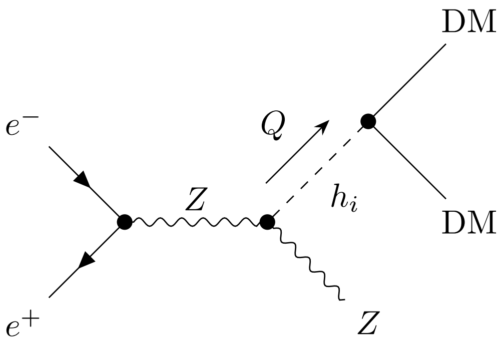

Figure 6. Feynman diagram for the considered channel of DM production. In the diagram, DM denotes the dark particle that is either A, X or ψ.

6 Production of DM pairs at future e^+e^- colliders

The DM models can be tested at e^+e^- collider experiments. In particular, these experiments allow for the copious production of DM states associated with a Z boson, what is referred to as so called Higgsstrahlung process or mono-Z emission [19, 20, 41–45], see figure 6. We assume that the energy of the Z boson can be reconstructed from data, therefore allowing for determination of the recoil mass ($\sqrt{Q^2}$), corresponding to the invariant mass of the dark particles.

JHEP08(2020)052

The differential cross section for DM pair production at e^+e^- colliders reads

$$\frac{d\sigma}{dQ^2} = \frac{\sigma_{\rm SM}(s,Q^2)\,v^2}{32\pi^2}\frac{\mathcal{X}\cdot\left(Q^2\right)^2}{\left[(Q^2-m_1^2)^2+(m_1\Gamma_1)^2\right]\left[(Q^2-m_2^2)^2+(m_2\Gamma_2)^2\right]}\times$$
$$\times\sqrt{1-4\frac{m_{\rm DM}^2}{Q^2}}\cdot\begin{cases}1 & \text{(pGDM)}\\ 1-4\frac{m_{\rm DM}^2}{Q^2}+12\left(\frac{m_{\rm DM}^2}{Q^2}\right)^2 & \text{(VDM)}\\ 2\frac{m_{\rm DM}^2}{Q^2}\left(1-4\frac{m_{\rm DM}^2}{Q^2}\right) & \text{(FDM)}\end{cases}, \tag{6.1}$$

where the parameter $\mathcal{X}$ is defined in eq. (5.2) and

$$\sigma_{\rm SM}(s,Q^2)\equiv\frac{g_V^2+g_A^2}{24\pi}\left(\frac{g^2}{\cos\theta_W^2}\frac{1}{s-m_Z^2}\right)^2\times$$
$$\times\frac{\lambda^{1/2}(s,Q^2,m_Z^2)\left[12\,s\,m_Z^2+\lambda(s,Q^2,m_Z^2)\right]}{8s^2} \tag{6.2}$$

is the cross section for the $e^+e^-\to Zh_{\rm SM}$ process, with mass of the SM Higgs particle equal to $\sqrt{Q^2}$. Here, $\lambda(a,b,c)$ denotes the Källén function, defined in appendix A, and g_V, g_A stand for the vector and axial coupling, respectively.[7] The above result has been obtained by adopting the standard Breit-Wigner propagators for the virtual/real Higgs bosons h_i.

Note that in the limit of $m_2\to m_1$ the cross section $d\sigma/dQ^2$ (6.1) seems to be amplified for h_i being on-shell, i.e. $Q^2\to m_{1,2}^2$. This is a surprising observation since, on the other hand, the second relation in (5.40) between masses and the portal coupling κ implies that in the limit $m_2\to m_1$, whenever $v_S\neq 0$, $\kappa\to 0$ so that the dark sector decouples in each model discussed here. Therefore, all cross sections for DM production or annihilation from the SM must vanish in this limit. Behaviour of the cross sections in this limit is potentially important phenomenologically, therefore in the following we are going to investigate the $Q^2\to m_{1,2}^2$ limit in more details.

Let's investigate the parameter $\mathcal{X}$. First, it is easy to see that

$$\lim_{m_2\to m_1}\mathcal{X}=\left[\sin 2\alpha\,\frac{m_1\,(\Gamma_1-\Gamma_2)}{2vv_S}\right]^2. \tag{6.3}$$

From (5.40) one finds that if $v_S\neq 0$ then the limit $m_2\to m_1$ implies $\kappa\to 0$ and $\lambda_H v^2-\lambda_S v_S^2\to 0$. Therefore, according to (2.7) $\tan 2\alpha$ is undefined. For instance, for fixed λ_H, v and v_S it is easy to see that, approaching the limiting point $(\lambda_H(v/v_S)^2,0)$ in the (λ_S,κ) plane, one can get $\alpha=0$, $\alpha=\pi/4$ or $\alpha=1/2\arctan(v/v_S)$, choosing the corresponding trajectories: $\kappa=0$, $\lambda_S=\lambda_H(v/v_S)^2$ or $\kappa=-\lambda_S+\lambda_H(v/v_S)^2$, respectively. Since in the limit $m_2\to m_1$ neither $\sin 2\alpha\to 0$ nor $\Gamma_1\to\Gamma_2$, so $\mathcal{X}$ does not vanish, in spite of justified arguments mentioned above. The solution to this puzzle lies in the fact that for $m_2\to m_1$ also off-diagonal ($i\neq j$) Higgs boson self-energies (see figure 7) are relevant and should be resummed so the naive, diagonal, Breit-Wigner propagators are not appropriate. To

---

[7] In the case of polarized beams, $g_V^2+g_A^2$ factor has to be replaced with $(1-P_+P_-)(g_V^2+g_A^2)$ $+2g_Vg_A(P_+-P_-)$, where $P_\pm$ denotes polarizations of $e^\pm$ beams.

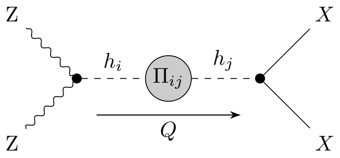

Figure 7. The Higgs-boson mediators with their self-energies.

illustrate this point let us consider the $e^+e^- \to ZXX$ process. The matrix element reads

$$\begin{aligned}\mathcal{M} &= \mathcal{M}_{e^+e^-\to Zh_i}(Q^2)\cdot\Delta_{ij}(Q^2)\cdot\mathcal{M}_{h_j\to XX}(Q^2) = \\ &= \mathcal{M}_{e^+e^-\to Zh}(Q^2)\cdot\underbrace{\mathcal{R}_{1i}\cdot\Delta_{ij}(Q^2)\cdot\mathcal{R}_{2j}}_{\widehat{\Delta}(Q^2)}\cdot\mathcal{M}_{h\to XX}(Q^2)\,. \end{aligned} \tag{6.4}$$

By $\widehat{\Delta}$ we denote the propagator contracted with the mixing matrix. From [46] (see also [47]), the contracted propagator can be expressed explicitly as

$$\begin{aligned}\widehat{\Delta}(Q^2) &= \mathcal{R}_{1i}\mathcal{R}_{2j}\cdot\frac{1}{\det D}\overbrace{\begin{bmatrix} Q^2-m_2^2+\Pi_{22} & -\Pi_{12} \\ -\Pi_{21} & s-m_1^2+\Pi_{11}\end{bmatrix}_{ij}}^{D} = \\ &= \sin\alpha\cos\alpha\cdot\frac{(m_1^2-m_2^2)-(\Pi_{11}-\Pi_{22})+(\tan\alpha\cdot\Pi_{12}-\cot\alpha\cdot\Pi_{21})}{(Q^2-m_1^2+\Pi_{11})(Q^2-m_2^2+\Pi_{22})-\Pi_{12}\Pi_{21}}\,,\end{aligned} \tag{6.5}$$

where $\Pi_{ij} \equiv \Pi_{ij}(Q^2)$ denotes the imaginary part (multiplied by i) of the h_ih_j self energy, satisfying $\Pi_{ii}(m_i^2) = im_i\Gamma_i$. In magnitude, all of them are comparable to $m_i\Gamma_i$. Results for Π_{ij} are collected in appendix A.

If $|m_1 - m_2| \gg \Gamma_1, \Gamma_2$, then the first term in the denominator, $(Q^2 - m_1^2 + \Pi_{11})$ $(Q^2-m_2^2+\Pi_{22})$, dominates for any Q^2, as well as the first term of the numerator, $(m_1^2-m_2^2)$. In such a case, the propagator can be approximated by

$$\widehat{\Delta}(Q^2) \simeq \sin\alpha\cos\alpha\cdot\frac{m_1^2-m_2^2}{(Q^2-m_1^2+\Pi_{11})(Q^2-m_2^2+\Pi_{22})}\,. \tag{6.6}$$

It is easy to see that the above propagator could be rewritten (dropping terms proportional to $\Gamma_{1,2}$ in the numerator) as

$$\widehat{\Delta}(Q^2) \simeq \widehat{\Delta}^{(BW)}(Q^2) \equiv \sin\alpha\cos\alpha\cdot\left[\frac{1}{Q^2-m_1^2+im_1\Gamma_1}-\frac{1}{Q^2-m_2^2+im_2\Gamma_2}\right], \tag{6.7}$$

which reduces to the standard Breit-Wigner propagator. This simplified result has to be replaced by the full formula whenever $|m_1 - m_2|$ is comparable to the widths. In order to investigate the case $m_1 \sim m_2$ one has to calculate Π_{ij}. The explicit calculation (see appendix A) confirms that

$$\left[(\Pi_{11}-\Pi_{22})-(\tan\alpha\cdot\Pi_{12}-\cot\alpha\cdot\Pi_{21})\right]\Big|_{m_1=m_2} = 0\,. \tag{6.8}$$

Hence, the full propagator (6.5) vanishes in the limit $m_1 = m_2$, exactly as it should. An important consequence of this result is that in the double-resonance region of $Q^2 \sim m_1^2 \sim m_2^2$, in the closest vicinity of $m_1 = m_2$, the straightforward application of the Breit-Wigner strategy is not appropriate.

However, in practice, the region $|m_1 - m_2| \lesssim \Gamma_{1,2}$ is so narrow that the naive Breit-Wigner approximated resummation (6.7) could be adopted, keeping in mind that exactly on the diagonal $m_1 = m_2$ the cross sections do vanish.

7 Constraints expected from future e^+e^- colliders

Production of the Standard Model Higgs boson in the Higgsstrahlung process is considered as a "golden channel" for a model independent determination of the Higgs boson properties at future e^+e^- colliders. By reconstructing the produced Z bozon, Higgsstrahlung events can be selected with high efficiency independently on the Higgs boson decay.

Largest sample of events can be selected when both leptonic and hadronic decay channels of the Z boson are considered. Reconstructing just the Z boson is of particular interest when we look for rare processes involving the Higgs boson, for instance possible decays into DM states. Events with mono-Z production, and no other activity in the detector, can be considered as candidate events for the invisible Higgs boson decays, if the recoil mass, $\sqrt{Q^2}$, reconstructed from energy-momentum conservation, is consistent with the Higgs boson mass. Highest sensitivity to invisible decays of the 125 GeV boson is expected at $\sqrt{s} \simeq 250\,\mathrm{GeV}$, corresponding to the maximum of the Higgsstrahlung cross section. The main background processes that limit the sensitivity at this energy range are the production of ZZ and W^+W^- pairs, as well as single Z production via the WW fusion, $e^+e^- \to \nu_e\bar{\nu}_e Z$. For the Z-boson pair production with one boson decaying into neutrinos, the final state reconstructed in the detector is identical to the one expected for the invisible Higgs boson decays and the recoil mass can be significantly overestimated due to beams spectra[8] or large initial state radiation. For hadronic Z-boson decays, also detector resolution effects, dominated by the jet energy resolution, are very important. Nevertheless, due to branching fraction much larger than in the leptonic case, the expected limits on the invisible decays of the 125 GeV Higgs boson are dominated by hadronic Z decay measurements. For 2000 fb^{-1} of data collected at 250 GeV ILC, the expected limit on the invisible branching fraction is 0.23%, when combining hadronic and leptonic channels [48]. Similar sensitivity is expected also for other future e^+e^- collider projects [49].

The Higgsstrahlung analysis can be extended to the search for production of a generic scalar of arbitrary mass, assuming it is produced in association with the Z boson, as described in the previous section. The analysis procedure is the same as for the 125 GeV Higgs boson, only the event selection criteria have to be tuned to the considered scalar mass. The cleanest sample of Higgsstrahlung events is obtained when selecting Z boson decaying into muons, as the invariant mass of the $\mu^+\mu^-$ pair can be reconstructed with sub-GeV

---

[8] At linear e^+e^- colliders the beamstrahlung effects result in the long tail in the beam energy spectra towards low energies. When the electron or positron participating in the collision has the initial energy much smaller than the nominal beam energy, the recoil mass can be significantly overestimated.

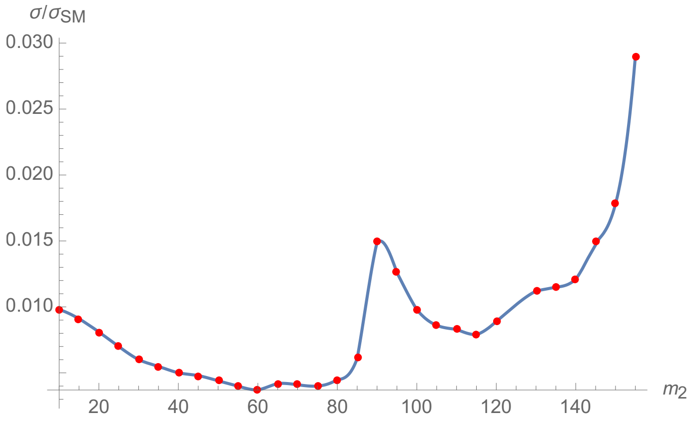

Figure 8. The 95% CL exclusion limits [18, 50, 51] on the cross section for $\sigma(e^+e^- \to Z+\cdots)/\sigma_{\rm SM}$ at the ILC at $\sqrt{s} = 250\,{\rm GeV}$ as a function of the mass of the extra Higgs boson h_2. The ellipsis denotes an undetected final state of invariant mass m_2. The SM cross section assumes $m_{h_{\rm SM}} = m_2$. Limits calculated using the CL(s) approach [53].

precision and the background levels are significantly smaller than for the hadronic channel. This channel gives the best sensitivity to the production of light scalars, below 125 GeV, as the hadronic background levels increase rapidly towards low recoil masses, and superior recoil mass reconstruction in muon channel allows for much better suppression of non-resonant background. No assumptions are made on the scalar decay modes or branching ratios. The expected number of events due to SM background processes remaining after the optimized selection cuts and the corresponding signal selection efficiency can be used to extract the expected cross-section limit on the new scalar production as a function of its mass. Shown in figure 8 are the 95% CL exclusion limits expected for the ILC running at $\sqrt{s} = 250\,{\rm GeV}$, normalized to the cross section for the SM Higgs boson production of a given mass [18, 50, 51]. Presented results assume Z-boson identification by its $\mu^+\mu^-$ decays only. In the frequentist approach, the limit value is defined as the signal production cross section which, with probability of 95%, would result in the observed number of events higher than the SM expectation. The sensitivity is weakest for the scalar mass close to the mass of the Z boson, due to the background from Z-boson pair production (with one Z decaying into muons). Scalar masses up to the kinematic limit of $\sqrt{s} - m_Z \sim 160\,{\rm GeV}$ can be probed at 250 GeV.

To extend the limits towards higher scalar masses, e^+e^- collider running at higher energies is needed. If the new scalar is heavier than 125 GeV and it is expected to decay predominantly in invisible channels, the cross-section limits can be improved by considering hadronic Z boson decays. This gives increase by a factor of 20 in the expected signal event statistics (compared to the $Z \to \mu^+\mu^-$ decay channel) with only moderate increase in background levels, as the mono-Z signature allows for efficient suppression of SM background processes [52].

8 Numerical results

Here we will apply the strategy described in earlier sections to investigate how large the total cross section for Z and DM production at an e^+e^- collider could be. In order to maximize the cross section we will focus on colliders running at the CoM energy close to $\sqrt{s} = 250\,\text{GeV}$, while drawing figures we specialize to the case of the ILC at exactly $\sqrt{s} = 250\,\text{GeV}$ [18, 50].

The cross section depends on four independent variables: m_2, m_{DM}, $\sin\alpha$ and v_S. Instead of v_S one can use $\mathcal{X}$ defined by (5.2), which is fixed by the relic abundance. Then, for each point (m_2, m_{DM}) in our plots, figures 9–13, we choose such a value of $\sin\alpha \leq 0.3$ that maximizes the cross section. Due to the resonant enhancement the cross section is much greater in the area where at least one of on-shell mediators $(h_{1,2})$ can decay into a pair of DM particles. As seen from (6.1), the differential cross section is maximized when the two Higgs bosons are on-shell at the same missing invariant mass $\sqrt{Q^2} \simeq m_1 \simeq m_2$. Therefore, the total cross section is largest when $m_1 \simeq m_2$. Hence, the maximum appears in the lower-left quarter as close to the diagonal $m_1 = m_2$ as allowed by the invisible-branching-ratio condition.[9] In the case of vector and fermion DM models, the direct detection limits on the DM-nucleon cross section are very strong, a consequence of that is that couplings between DM and the SM (parametrized by $\mathcal{X}$) must be severely suppressed. Therefore, in general, in order to satisfy the DD constraint and at the same time provide appropriate DM abundance, the early-Universe DM annihilation must occur in a vicinity of a resonance, i.e. either $2m_{\text{DM}} - m_1 \simeq 0$ or $2m_{\text{DM}} - m_2 \simeq 0$. For the pGDM, because of the natural suppression of the DD cross section (which is vanishing at the tree level in the limit of zero momentum transfer, see section 5.3), the resonant annihilation is not necessary to reproduce the correct DM abundance. Nevertheless, to compare the models, we have found it convenient to plot the cross section in the space spanned by $m_{\text{DM}} - m_1/2$ and $m_{\text{DM}} - m_2/2$ in the vicinity of the resonance, i.e. $m_{\text{DM}} \simeq m_1/2$ and/or $m_{\text{DM}} \simeq m_2/2$. The DM and h_2 masses adopted hereafter satisfy the following constraints

$$\left| m_{\text{DM}} - \frac{m_{1,2}}{2} \right| < 5\,\text{GeV} \tag{8.1}$$

what implies that $57.5\,\text{GeV} < m_{\text{DM}} < 67.5\,\text{GeV}$ and $105\,\text{GeV} < m_2 < 145\,\text{GeV}$.[10]

In figures 9–10 we plot maximized cross section for the Z and DM production (normalized to the SM prediction for the Zh_{SM} production, i.e. $\sigma_{\text{SM}} = \sigma(e^+e^- \to Zh_{\text{SM}})|_{m_{h_{\text{SM}}}=m_1}$) at the ILC for pGDM, VDM and FDM models, respectively. The greenish colors denote regions where the models satisfy adopted constraints showing (by color) the corresponding cross section. The cyan marks regions excluded by the SM invisible BR limit, $\text{BR}(h_1 \to \text{DM}) < 0.19$, while the black corresponds to parameters excluded by the DD limit (see section 5.3). As explained earlier, the allowed regions for the VDM and the FDM models appear in the vicinity of resonant DM annihilation. For the gray region, the

---

[9] It should be remembered that in the closest vicinity of $m_1 = m_2$ one should adopt the results discussed at the end of section 6. However, with the resolution adopted to draw plots in this paper those effects are invisible.

[10] Region in (m_{DM}, m_2) plane that corresponds to (8.1) is *not* a rectangle.

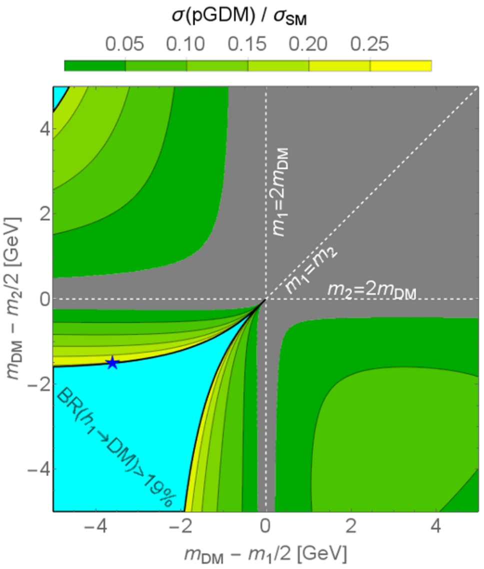

benchmark point for pGDM

$m_2 = 120.8\,\mathrm{GeV}\,,$ $m_{\mathrm{DM}} = 58.9\,\mathrm{GeV}\,,$

$\sin\alpha = 0.30\,,$ $v_S = 646\,\mathrm{GeV}\,,$

$\Gamma_1 = 7.4\cdot 10^{-3}\,\mathrm{GeV}\,,$ $\Gamma_2 = 9.8\cdot 10^{-3}\,\mathrm{GeV}\,,$

$\mathrm{BR}(h_1 \to \mathrm{DM}) = 19\%\,,$ $\mathrm{BR}(h_2 \to \mathrm{DM}) = 95\%\,,$

$\sigma = 62$ fb

Figure 9. The figure shows, for the pGDM, the allowed region (greenish), the region forbidden by the invisible BR of h_1 (cyan) where $\mathrm{BR}(h_1 \to \mathrm{DM}) > 19\%$ and the gray region where the normalized cross section falls below its expected precision at the 95% CL shown in figure 8. Coloring of the greenish area, explained in the legend, shows the value of the normalized total cross section σ/σ_{SM}. The star denotes the chosen benchmark point, characterized by relatively high cross section.

expected 95% CL sensitivity limit for $\sigma/\sigma_{\mathrm{SM}}$ (shown in figure 8) is above the $\sigma/\sigma_{\mathrm{SM}}$ prediction. Therefore, one can conclude that the greenish regions are those which are detectable at the ILC, assuming that the $\sin\alpha$ is close to the value that maximizes the cross section. It turns out that usually the $\sin\alpha$ that provides maximal cross section is just at the largest value allowed by the LHC Higgs signal measurement, $\sin\alpha \simeq 0.3$. The fair conclusion from inspecting figures 9–10 is that in the substantial part of the parameter range that was shown, the DM production can be detected at future e^+e^- colliders running around $\sqrt{s} = 250\,\mathrm{GeV}$.

The simplest and straightforward way to disentangle the models is to measure m_2 and m_{DM} and then verify if the measured masses are consistent with any of the discussed models after imposing constraints. In other words, one would need to check if for the measured values of m_2 and m_{DM} the corresponding point $(m_{\mathrm{DM}} - m_1/2, m_{\mathrm{DM}} - m_2/2)$ is located in the greenish area in any of figures 9–10. In order to facilitate and illustrate the verification, we have made plots shown in figure 11. The upper-left panel shows the cyan region where the pGDM is excluded by the h_1-invisible-BR condition, while the white region is allowed. In the upper-right panel the yellow regions denote region where the FDM model is disallowed, while white color stands again for region that agrees with all the constraints. Similarly, the lower-left panel shows forbidden (magenta) and allowed (white) regions for the VDM model. The lower-right plot combines results for all the models; again, white denotes the region where all the models are allowed. As it is seen, there exist regions where two or even three models coexist. However, there is also, in the lower-right panel, the magenta region where only the pGDM may exist. Therefore, the very first step

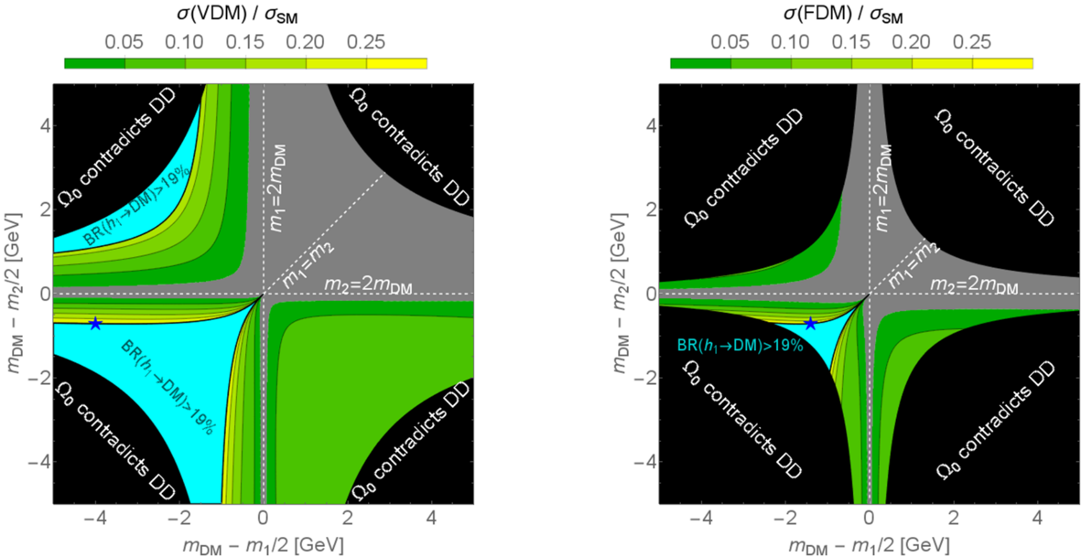

benchmark point for VDM

$m_2 = 118.4\,\mathrm{GeV}\,,\qquad m_{\mathrm{DM}} = 58.5\,\mathrm{GeV}\,,$
$\sin\alpha = 0.30\,,\qquad v_S = 561\,\mathrm{GeV}\,,$
$\Gamma_1 = 7.4\cdot 10^{-3}\,\mathrm{GeV}\,,\qquad \Gamma_2 = 6.4\cdot 10^{-3}\,\mathrm{GeV}\,,$
$\mathrm{BR}(h_1\to \mathrm{DM}) = 18\%\,,\qquad \mathrm{BR}(h_2\to \mathrm{DM}) = 92\%\,,$
$\sigma = 61$ fb

benchmark point for FDM

$m_2 = 123.6\,\mathrm{GeV}\,,\qquad m_{\mathrm{DM}} = 61.1\,\mathrm{GeV}\,,$
$\sin\alpha = 0.30\,,\qquad v_S = 76\,\mathrm{GeV}\,,$
$\Gamma_1 = 7.4\cdot 10^{-3}\,\mathrm{GeV}\,,\qquad \Gamma_2 = 5.9\cdot 10^{-3}\,\mathrm{GeV}\,,$
$\mathrm{BR}(h_1\to \mathrm{DM}) = 18\%\,,\qquad \mathrm{BR}(h_2\to \mathrm{DM}) = 91\%\,,$
$\sigma = 59$ fb

Figure 10. As in figure 9 for the VDM model (left) and the FDM model (right). The region forbidden by the DD constraint is denoted by black color.

in an attempt to disentangle the models should be a measurement of m_2 and m_{DM} and its verification against the results shown in figure 11. Even though there is a substantial region of full degeneracy (white), there exists also significant area where some valuable conclusions could be drawn. It is even conceivable that this measurement would be consistent with the spin 0 (pGDM) hypothesis only.

Now, we would like to focus on estimating chances to disentangle pairs of the models by the measurement of the normalized cross section $\sigma/\sigma_{\mathrm{SM}}$. In order to verify this option, we plot (figures 12 and 13) differences between model predictions and compare them against the expected experimental precision given by the limit provided by figure 8. As previously, it turns out that the highest differences are obtained for $\sin\alpha$ as large as allowed, i.e. $\sin\alpha \simeq 0.3$. More reddish color indicate parameter regions for which models that are being compared are easier to disentangle since there an absolute value of the corresponding difference of cross sections is larger. It is clear that the disentanglement is a very ambitious task. It seems that only the VDM and the pGDM could be relatively easily disentangled by the measurement of $e^+e^- \to Z + \cdots$ cross section at future e^+e^- colliders operating near $\sqrt{s} = 250\,\mathrm{GeV}$ if the parameters are in the more reddish regions of figure 12.

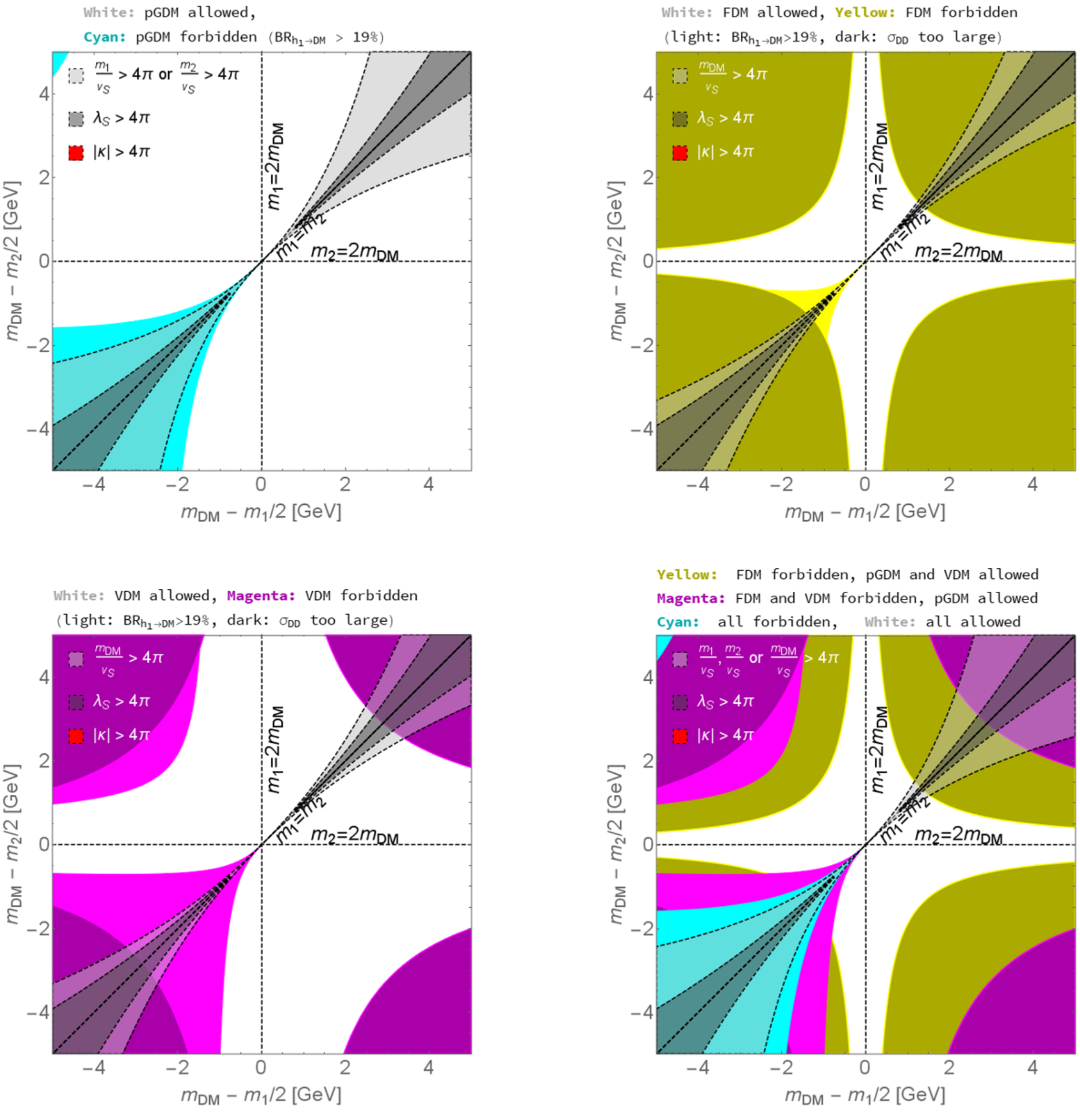

Figure 11. The parameter space allowed or forbidden for the discussed models. Top-left: pGDM model, top-right: FDM model, bottom-left: VDM model, bottom-right: the three models combined. Light- and dark-gray regions denote violation of perturbativity conditions (5.14). Note that the $|\kappa| < 4\pi$ condition is not violated in any place of the considered range of parameters.

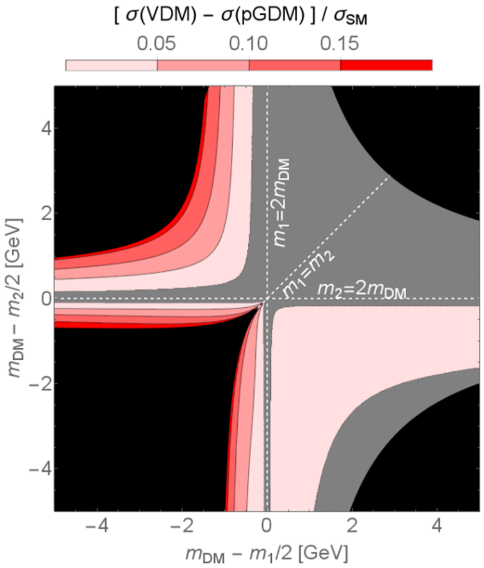

Figure 12. The difference between predictions for the pGDM and the VDM. The gray region denotes parameter space for which the difference is smaller than the limit of figure 8. The models are compared in the region where both of them are consistent with the data, see figure 11.

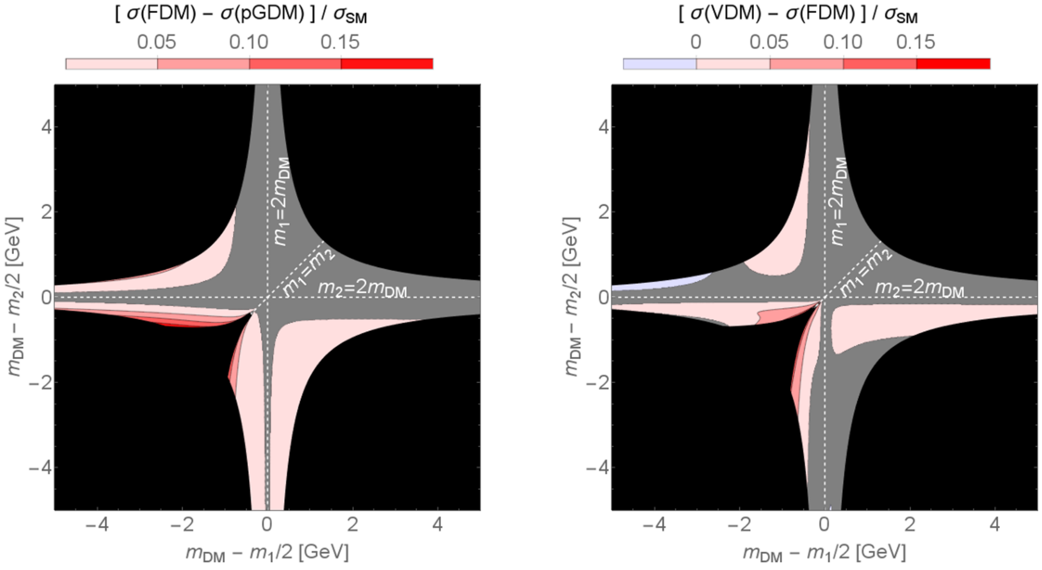

Figure 13. The difference between predictions for the pGDM and the FDM (left panel), and the FDM and the VDM (right panel). The gray region denotes parameter space for which the difference is smaller than the limit of figure 8. The models are compared in the region where both of them are consistent with the data, see figure 11.

9 Summary

In this analysis, our goal was to investigate how could one disentangle models of dark matter of different spin at future e^+e^- colliders operating near $\sqrt{s} = 250\,\text{GeV}$. For that purpose, we adopted the ILC project with the CoM energy at $\sqrt{s} = 250\,\text{GeV}$. Our strategy was pragmatic and phenomenological. We considered three nearly simplest models of dark matter of spin 0, 1 and $1/2$. The models adopted here were not the "simplified" ones, discussed often in a phenomenological literature on dark matter; in contrast, they were simple but attractive, consistent and renormalizable quantum field theories. In spite of dark-matter-spin differences, the models considered here share exactly the same parameter space, so the comparison point by point was meaningful. It turned out that the most promising region of the parameter space is located near the double resonance $2m_{\text{DM}} \sim m_{1,2}$. It has been shown that in this region, in the closest vicinity of $m_1 = m_2$, the naive Breit-Wigner strategy must be replaced by a proper resummation of 1-loop Higgs-boson self-energies that takes into account their off-diagonal elements.

In order to verify if a model was testable, we had adopted expected 95% CL sensitivity for the measurement of the $e^+e^- \to Z + \cdots$ cross section obtained for the ILC project. It has been assumed that only the Z boson is reconstructed without any other detector activity. Predictions of the models were calculated taking into account the dark matter abundance, indirect and direct detection experiments and the collider constraints on the Higgs-boson invisible branching ratio and limits on the mixing angle (present in all the models). That way, regions of the parameter space where the cross section would be measurable were obtained for each of the models. We have also discussed the possibility to disentangle the models by a measurement of the cross section. It turned out that the most optimistic case is the detection of differences between the pseudo-Goldstone dark matter (spin 0) and the vector dark matter (spin 1). Regions of the parameter space where no model is allowed or some models could coexist were also determined.

Acknowledgments

The work was partially supported by the National Science Centre (Poland) OPUS research projects under contracts nos. UMO-2017/25/B/ST2/00191 and UMO-2017/25/B/ST2/00496, and HARMONIA project under contract no. UMO-2015/18/M/ST2/00518 (2016–2019).

A Higgs boson self-energies and decay widths

Here we collect results for imaginary parts of two-point functions $\Pi_{ij}(Q^2)$ for Higgs bosons $h_{i,j}$. Each self-energy is a sum of contributions of loops with various intermediate states[11] being on-shell:

$$\Pi_{ij} = \Pi_{ij}^{\text{DM}} + \Pi_{ij}^{W^+W^-} + \Pi_{ij}^{ZZ} + \sum_q \Pi_{ij}^{q\bar{q}} + \sum_l \Pi_{ij}^{l^+l^-} + \sum_{k,l} \Pi_{ij}^{h_k h_l}\,, \tag{A.1}$$

---

[11] We omit tadpole and seagull diagrams.

where DM stands for dark matter particle A, X or ψ while q denotes SM quarks and l denotes SM leptons. These contributions are given by (see [46] for the VDM case[12]):

$$\begin{aligned}\Pi_{ij}^{\rm DM}(Q^2) &= I(Q^2, m_{\rm DM}, m_{\rm DM})\frac{\mathcal{R}_{2i}\mathcal{R}_{2j}}{32\pi^2 v_S^2}(m_i m_j)^2\times\\ &\quad\times\begin{cases}1 & \text{(pGDM)}\\ 1-2\,m_{\rm DM}^2\frac{4Q^2-m_i^2-m_j^2}{(m_im_j)^2}+12\left(\frac{m_{\rm DM}^2}{(m_im_j)^2}\right)^2 & \text{(VDM)}\\ 2\frac{m_{\rm DM}^2Q^2}{(m_im_j)^2}\left(1-4\frac{m_{\rm DM}^2}{Q^2}\right) & \text{(FDM)}\end{cases}, \qquad \text{(A.2)}\end{aligned}$$

$$\begin{aligned}\Pi_{ij}^{W^+W^-}(Q^2) &= I(Q^2, m_W, m_W)\frac{\mathcal{R}_{1i}\mathcal{R}_{1j}}{16\pi^2 v^2}(m_i m_j)^2\times\\ &\quad\times\left[1-2m_W^2\frac{4Q^2-m_i^2-m_j^2}{(m_im_j)^2}+12\frac{m_W^4}{(m_im_j)^2}\right], \qquad \text{(A.3)}\end{aligned}$$

$$\begin{aligned}\Pi_{ij}^{ZZ}(Q^2) &= I(Q^2, m_Z, m_Z)\frac{\mathcal{R}_{1i}\mathcal{R}_{1j}}{32\pi^2 v^2}(m_i m_j)^2\times\\ &\quad\times\left[1-2m_Z^2\frac{4Q^2-m_i^2-m_j^2}{(m_im_j)^2}+12\frac{m_Z^4}{(m_im_j)^2}\right], \qquad \text{(A.4)}\end{aligned}$$

$$\Pi_{ij}^{q\bar{q}}(Q^2) = I(Q^2, m_q, m_q)\cdot\frac{3\mathcal{R}_{1i}\mathcal{R}_{1j}}{8\pi^2 v^2}m_q^2Q^2\left(1-4\frac{m_q^2}{Q^2}\right), \qquad \text{(A.5)}$$

$$\Pi_{ij}^{l^+l^-}(Q^2) = I(Q^2, m_l, m_l)\cdot\frac{\mathcal{R}_{1i}\mathcal{R}_{1j}}{8\pi^2 v^2}m_l^2Q^2\left(1-4\frac{m_l^2}{Q^2}\right), \qquad \text{(A.6)}$$

$$\Pi_{ij}^{h_kh_l}(Q^2) = I(Q^2, m_k, m_l)\cdot\frac{V_{ikl}V_{jkl}}{32\pi^2}, \qquad \text{(A.7)}$$

where

$$V_{111} \equiv 3m_1^2\left(\frac{\sin^3\alpha}{v_S}+\frac{\cos^3\alpha}{v}\right), \qquad \text{(A.8)}$$

$$V_{112} = V_{121} = V_{211} \equiv (2m_1^2+m_2^2)\sin\alpha\cos\alpha\left(\frac{\sin\alpha}{v_S}-\frac{\cos\alpha}{v}\right), \qquad \text{(A.9)}$$

$$V_{221} = V_{212} = V_{122} \equiv (m_1^2+2m_2^2)\sin\alpha\cos\alpha\left(\frac{\cos\alpha}{v_S}+\frac{\sin\alpha}{v}\right), \qquad \text{(A.10)}$$

$$V_{222} \equiv 3m_2^2\left(\frac{\cos^3\alpha}{v_S}-\frac{\sin^3\alpha}{v}\right) \qquad \text{(A.11)}$$

are the couplings corresponding to the $h_ih_jh_k$ vertices $(i,j,k=1,2)$ [46] and

$$\begin{aligned}I(Q^2, m_a, m_b) &\equiv i\cdot\mathrm{Im}\left[B_0(Q^2, m_a^2, m_b^2)\right] =\\ &= i\cdot\mathrm{Im}\left[\frac{1}{i\pi^2}\int\frac{d^4l}{(l^2-m_a^2)[(l+Q)^2-m_b^2]}\right] =\\ &= i\pi\cdot\frac{\lambda^{1/2}(Q^2, m_a^2, m_b^2)}{Q^2}\cdot\mathbb{1}_{Q^2>(m_a+m_b)^2} \qquad \text{(A.12)}\\ \Rightarrow\quad I(Q^2, m, m) &= i\pi\cdot\sqrt{1-\frac{4m^2}{Q^2}}\cdot\mathbb{1}_{Q^2>4m^2}\end{aligned}$$

---

[12] In [46], there is an additional i factor in the definition of V_{ijk}, hence additional minus in their version of eq. (A.7).

are imaginary parts[13] (times i) of appropriate loop integrals B_0 [54], where λ denotes the Källén function, defined as

$$\lambda(a,b,c) \equiv a^2+b^2+c^2-2(ab+bc+ca)\,. \tag{A.13}$$

By straightforward calculations it can be shown that

$$\left[\left(\Pi^{ab}_{11}-\Pi^{ab}_{22}\right)-\left(\tan\alpha\cdot\Pi^{ab}_{12}-\cot\alpha\cdot\Pi^{ab}_{21}\right)\right]\Big|_{m_1=m_2}=0 \tag{A.14}$$

for $ab=\mathrm{DM}$, W^+W^-, ZZ, $q\bar{q}$, l^+l^-, h_kh_l (in the last case one has to sum over $k,l=1,2$). Hence, also the sum over all contributions vanishes in this limit:

$$\left[(\Pi_{11}-\Pi_{22})-(\tan\alpha\cdot\Pi_{12}-\cot\alpha\cdot\Pi_{21})\right]\Big|_{m_1=m_2}=0\,. \tag{A.15}$$

The h_1's and h_2's partial widths can be calculated as

$$\Gamma_{h_i\to ab}=\frac{\Pi^{ab}_{ii}(m_i^2)}{im_i}\,.$$

The widths relevant for this project are therefore given by

$$\begin{aligned}
\Gamma_{h_i\to\mathrm{DM}} &= \frac{\mathcal{R}^2_{2i}}{v_S^2}\frac{m_i^3}{32\pi}\sqrt{1-\frac{4m^2_{\mathrm{DM}}}{m_i^2}}\times\\
&\quad\times\begin{cases}1 & \text{(pGDM)}\\ 1-4\frac{m^2_{\mathrm{DM}}}{m_i^2}+12\left(\frac{m^2_{\mathrm{DM}}}{m_i^2}\right)^2 & \text{(VDM)}\\ 2\frac{m^2_{\mathrm{DM}}}{m_i^2}\left(1-4\frac{m^2_{\mathrm{DM}}}{m_i^2}\right) & \text{(FDM)}\end{cases}\,, && \text{(A.16)}\\
\Gamma_{h_i\to\mathrm{SM}} &= \mathcal{R}^2_{1i}\cdot\gamma(m_i) && \text{(A.17)}\\
&\quad(\gamma\text{ denotes the decay width of SM Higgs particle of given mass})\,,\\
\Gamma_{h_1\to h_2h_2} &= \sin^2\alpha\,\cos^2\alpha\,(m_1^2+2m_2^2)^2\left(\frac{\cos\alpha}{v_S}+\frac{\sin\alpha}{v}\right)^2\frac{\sqrt{m_1^2-4m_2^2}}{32\pi m_1^2}\simeq\\
&\simeq\frac{\sin^2\alpha\,\cos^4\alpha}{v_S^2}(m_1^2+2m_2^2)^2\frac{\sqrt{m_1^2-4m_2^2}}{32\pi m_1^2}\,, && \text{(A.18)}\\
\Gamma_{h_2\to h_1h_1} &= \sin^2\alpha\,\cos^2\alpha\,(2m_1^2+m_2^2)^2\left(\frac{\sin\alpha}{v_S}-\frac{\cos\alpha}{v}\right)^2\frac{\sqrt{m_2^2-4m_1^2}}{32\pi m_2^2}\simeq\\
&\simeq\frac{\sin^2\alpha\,\cos^4\alpha}{v^2}(2m_1^2+m_2^2)^2\frac{\sqrt{m_2^2-4m_1^2}}{32\pi m_2^2}\,. && \text{(A.19)}
\end{aligned}$$

---

[13] The choice of the sign depends on the corresponding choice in $\ln(-1)=\pm i\pi$. We want the imaginary part to be positive, since it corresponds to the correct asymptotic value, i.e. $\Pi_{ii}(m_i^2)=+im_i\Gamma_i$.

B Passarino-Veltman functions

Functions used in eq. (5.8) are defined in terms of Passarino-Veltman functions [54]:

$$D(0,0,\sqrt{p^2};m_a,m_b,m_c,m_d) \equiv \frac{p^\mu}{p^2} D_\mu(0,0,p;m_a,m_b,m_c,m_d)\,, \tag{B.1}$$

$$C(0,\sqrt{p^2};m_a,m_b,m_c) \equiv \frac{p^\mu}{p^2} C_\mu(0,p;m_a,m_b,m_c)\,. \tag{B.2}$$

Explicit values are:

$$\begin{aligned} &D(0,0,m_{\rm DM};m_1,m_1,m_2,m_{\rm DM}) = \\ &\quad= \frac{p^\mu}{m_{\rm DM}^2}\frac{1}{i\pi^2}\int d^4l \frac{l_\mu}{(l^2-m_1^2)^2(l^2-m_2^2)\left[(l+p)^2-m_{\rm DM}^2\right]}\bigg|_{p^2=m_{\rm DM}^2} = \\ &\quad= \frac{1}{m_1^2-m_2^2}\left[C(0,m_{\rm DM};m_1,m_1,m_{\rm DM}) - C(0,m_{\rm DM};m_1,m_2,m_{\rm DM})\right]\,, \end{aligned} \tag{B.3}$$

$$\begin{aligned} &D(0,0,m_{\rm DM};m_1,m_2,m_2,m_{\rm DM}) = \\ &\quad= \frac{p^\mu}{m_{\rm DM}^2}\frac{1}{i\pi^2}\int d^4l \frac{l_\mu}{(l^2-m_1^2)(l^2-m_2^2)^2\left[(l+p)^2-m_{\rm DM}^2\right]}\bigg|_{p^2=m_{\rm DM}^2} = \\ &\quad= -\frac{1}{m_1^2-m_2^2}\left[C(0,m_{\rm DM};m_2,m_2,m_{\rm DM}) - C(0,m_{\rm DM};m_1,m_2,m_{\rm DM})\right]\,, \end{aligned} \tag{B.4}$$

$$\begin{aligned} &C(0,m_{\rm DM};m_1,m_2,m_{\rm DM}) = \\ &\quad= \frac{p^\mu}{m_{\rm DM}^2}\frac{1}{i\pi^2}\int d^4l \frac{l_\mu}{(l^2-m_1^2)(l^2-m_2^2)\left[(l+p)^2-m_{\rm DM}^2\right]}\bigg|_{p^2=m_{\rm DM}^2} = \\ &\quad= \frac{1}{m_1^2-m_2^2}\left[B(m_{\rm DM};m_1,m_{\rm DM}) - B(m_{\rm DM};m_2,m_{\rm DM})\right]\,, \end{aligned} \tag{B.5}$$

where the following auxiliary functions are used:

$$\begin{aligned} &C(0,m_{\rm DM};m_i,m_i,m_{\rm DM}) = \\ &\quad= -\frac{1}{m_{\rm DM}^2}\left[1+\frac{x_i^+(x_i^+-1)}{x_i^+-x_i^-}\ln\left(\frac{x_i^+-1}{x_i^+}\right) - \frac{x_i^-(x_i^--1)}{x_i^+-x_i^-}\ln\left(\frac{x_i^--1}{x_i^-}\right)\right]\,, \end{aligned} \tag{B.6}$$

$$\begin{aligned} &B(m_{\rm DM};m_i,m_{\rm DM}) = \\ &\quad= -\frac{1}{2}\left[\left(\frac{2}{\epsilon}-\gamma+\ln\frac{\mu^2}{m_{\rm DM}^2}\right)+\right. \\ &\qquad\qquad \left. +1+\frac{m_i^2}{m_{\rm DM}^2}+(x_i^+)^2\ln\left(\frac{x_i^+-1}{x_i^+}\right)+(x_i^-)^2\ln\left(\frac{x_i^--1}{x_i^-}\right)\right]\,, \end{aligned} \tag{B.7}$$

$$x_i^\pm \equiv \frac{m_i^2 \pm \sqrt{m_i^4 - 4m_i^2 m_{\rm DM}^2}}{2m_{\rm DM}^2}\,. \tag{B.8}$$

The $\left(\frac{2}{\epsilon}-\gamma+\ln\frac{\mu^2}{m_{\rm DM}^2}\right)$ term present in eq. (B.7) appears due to the chosen regularization scheme and cancels out in eq. (B.5).

References

[1] ATLAS collaboration, *Combined search for the Standard Model Higgs boson using up to* $4.9\,fb^{-1}$ *of pp collision data at* $\sqrt{s} = 7$ *TeV with the ATLAS detector at the LHC*, *Phys. Lett. B* **710** (2012) 49 [`arXiv:1202.1408`] [INSPIRE].

[2] CMS collaboration, *Combined results of searches for the standard model Higgs boson in pp collisions at* $\sqrt{s} = 7$ *TeV*, *Phys. Lett. B* **710** (2012) 26 [`arXiv:1202.1488`] [INSPIRE].

[3] F. Zwicky, *Die Rotverschiebung von extragalaktischen Nebeln*, *Helv. Phys. Acta* **6** (1933) 110 [INSPIRE].

[4] E. Corbelli and P. Salucci, *The Extended Rotation Curve and the Dark Matter Halo of M33*, *Mon. Not. Roy. Astron. Soc.* **311** (2000) 441 [`astro-ph/9909252`] [INSPIRE].

[5] A. Dar, J. Goldberg and M. Rudzsky, *Dark matter and big bang nucleosynthesis*, `astro-ph/9405010` [INSPIRE].

[6] D. Clowe, A. Gonzalez and M. Markevitch, *Weak lensing mass reconstruction of the interacting cluster 1E0657-558: Direct evidence for the existence of dark matter*, *Astrophys. J.* **604** (2004) 596 [`astro-ph/0312273`] [INSPIRE].

[7] G. Bertone, D. Hooper and J. Silk, *Particle dark matter: Evidence, candidates and constraints*, *Phys. Rept.* **405** (2005) 279 [`hep-ph/0404175`] [INSPIRE].

[8] M. Bartelmann and P. Schneider, *Weak gravitational lensing*, *Phys. Rept.* **340** (2001) 291 [`astro-ph/9912508`] [INSPIRE].

[9] Y. Sofue and V. Rubin, *Rotation curves of spiral galaxies*, *Ann. Rev. Astron. Astrophys.* **39** (2001) 137 [`astro-ph/0010594`] [INSPIRE].

[10] PLANCK collaboration, *Planck 2015 results. XIII. Cosmological parameters*, *Astron. Astrophys.* **594** (2016) A13 [`arXiv:1502.01589`] [INSPIRE].

[11] WMAP collaboration, *Nine-Year Wilkinson Microwave Anisotropy Probe (WMAP) Observations: Cosmological Parameter Results*, *Astrophys. J. Suppl.* **208** (2013) 19 [`arXiv:1212.5226`] [INSPIRE].

[12] FCC collaboration, *FCC-ee: The Lepton Collider*: Future Circular Collider Conceptual Design Report Volume 2, *Eur. Phys. J. ST* **228** (2019) 261 [INSPIRE].

[13] A. Blondel et al., *Theory Requirements and Possibilities for the FCC-ee and other Future High Energy and Precision Frontier Lepton Colliders*, `arXiv:1901.02648` [INSPIRE].

[14] N. Alipour Tehrani et al., *FCC-ee: Your Questions Answered*, in *CERN Council Open Symposium on the Update of European Strategy for Particle Physics*, A. Blondel and P. Janot eds. (2019) [`arXiv:1906.02693`] [INSPIRE].

[15] CEPC STUDY GROUP collaboration, *CEPC Conceptual Design Report: Volume 2 — Physics & Detector*, `arXiv:1811.10545` [INSPIRE].

[16] K. Fujii et al., *The Potential of the ILC for Discovering New Particles*, `arXiv:1702.05333` [INSPIRE].

[17] K. Fujii et al., *Physics Case for the* 250 *GeV Stage of the International Linear Collider*, `arXiv:1710.07621` [INSPIRE].

[18] P. Bambade et al., *The International Linear Collider: A Global Project*, arXiv:1903.01629 [INSPIRE].

[19] T. Kamon, P. Ko and J. Li, *Characterizing Higgs portal dark matter models at the ILC*, *Eur. Phys. J. C* **77** (2017) 652 [arXiv:1705.02149] [INSPIRE].

[20] P. Ko and H. Yokoya, *Search for Higgs portal DM at the ILC*, *JHEP* **08** (2016) 109 [arXiv:1603.04737] [INSPIRE].

[21] V. Silveira and A. Zee, *Scalar phantoms*, *Phys. Lett. B* **161** (1985) 136 [INSPIRE].

[22] J. McDonald, *Gauge singlet scalars as cold dark matter*, *Phys. Rev. D* **50** (1994) 3637 [hep-ph/0702143] [INSPIRE].

[23] S. Pokorski, *Gauge field theories*, Cambridge University Press (2005).

[24] M. Gonderinger, H. Lim and M.J. Ramsey-Musolf, *Complex Scalar Singlet Dark Matter: Vacuum Stability and Phenomenology*, *Phys. Rev. D* **86** (2012) 043511 [arXiv:1202.1316] [INSPIRE].

[25] V. Barger, M. McCaskey and G. Shaughnessy, *Complex Scalar Dark Matter vis-à-vis CoGeNT, DAMA/LIBRA and XENON100*, *Phys. Rev. D* **82** (2010) 035019 [arXiv:1005.3328] [INSPIRE].

[26] V. Barger, P. Langacker, M. McCaskey, M. Ramsey-Musolf and G. Shaughnessy, *Complex Singlet Extension of the Standard Model*, *Phys. Rev. D* **79** (2009) 015018 [arXiv:0811.0393] [INSPIRE].

[27] D. Azevedo, M. Duch, B. Grzadkowski, D. Huang, M. Iglicki and R. Santos, *Testing scalar versus vector dark matter*, *Phys. Rev. D* **99** (2019) 015017 [arXiv:1808.01598] [INSPIRE].

[28] T. Hambye, *Hidden vector dark matter*, *JHEP* **01** (2009) 028 [arXiv:0811.0172] [INSPIRE].

[29] O. Lebedev, H.M. Lee and Y. Mambrini, *Vector Higgs-portal dark matter and the invisible Higgs*, *Phys. Lett. B* **707** (2012) 570 [arXiv:1111.4482] [INSPIRE].

[30] Y. Farzan and A.R. Akbarieh, *VDM: A model for Vector Dark Matter*, *JCAP* **10** (2012) 026 [arXiv:1207.4272] [INSPIRE].

[31] S. Baek, P. Ko, W.-I. Park and E. Senaha, *Higgs Portal Vector Dark Matter: Revisited*, *JHEP* **05** (2013) 036 [arXiv:1212.2131] [INSPIRE].

[32] S. Baek, P. Ko and W.-I. Park, *Invisible Higgs Decay Width vs. Dark Matter Direct Detection Cross Section in Higgs Portal Dark Matter Models*, *Phys. Rev. D* **90** (2014) 055014 [arXiv:1405.3530] [INSPIRE].

[33] M. Duch, B. Grzadkowski and M. McGarrie, *A stable Higgs portal with vector dark matter*, *JHEP* **09** (2015) 162 [arXiv:1506.08805] [INSPIRE].

[34] A. Freitas, S. Westhoff and J. Zupan, *Integrating in the Higgs Portal to Fermion Dark Matter*, *JHEP* **09** (2015) 015 [arXiv:1506.04149] [INSPIRE].

[35] FERMI-LAT and DES collaborations, *Searching for Dark Matter Annihilation in Recently Discovered Milky Way Satellites with Fermi-LAT*, *Astrophys. J.* **834** (2017) 110 [arXiv:1611.03184] [INSPIRE].

[36] D. Azevedo, M. Duch, B. Grzadkowski, D. Huang, M. Iglicki and R. Santos, *One-loop contribution to dark-matter-nucleon scattering in the pseudo-scalar dark matter model*, *JHEP* **01** (2019) 138 [arXiv:1810.06105] [INSPIRE].

[37] C. Gross, O. Lebedev and T. Toma, *Cancellation Mechanism for Dark-Matter-Nucleon Interaction*, *Phys. Rev. Lett.* **119** (2017) 191801 [arXiv:1708.02253] [INSPIRE].

[38] XENON collaboration, *Dark Matter Search Results from a One Ton-Year Exposure of XENON1T*, Phys. Rev. Lett. **121** (2018) 111302 [`arXiv:1805.12562`] [INSPIRE].

[39] W.-F. Chang, T. Modak and J.N. Ng, *Signal for a light singlet scalar at the LHC*, Phys. Rev. D **97** (2018) 055020 [`arXiv:1711.05722`] [INSPIRE].

[40] CMS collaboration, *Search for invisible decays of a Higgs boson produced through vector boson fusion in proton-proton collisions at $\sqrt{s} = 13$ TeV*, Phys. Lett. B **793** (2019) 520 [`arXiv:1809.05937`] [INSPIRE].

[41] H. Dreiner, M. Huck, M. Krämer, D. Schmeier and J. Tattersall, *Illuminating Dark Matter at the ILC*, Phys. Rev. D **87** (2013) 075015 [`arXiv:1211.2254`] [INSPIRE].

[42] Z.-H. Yu, X.-J. Bi, Q.-S. Yan and P.-F. Yin, *Dark matter searches in the mono-Z channel at high energy e^+e^- colliders*, Phys. Rev. D **90** (2014) 055010 [`arXiv:1404.6990`] [INSPIRE].

[43] N. Wan, M. Song, G. Li, W.-G. Ma, R.-Y. Zhang and J.-Y. Guo, *Searching for dark matter via mono-Z boson production at the ILC*, Eur. Phys. J. C **74** (2014) 3219 [`arXiv:1403.7921`] [INSPIRE].

[44] J. Liu, X.-P. Wang and F. Yu, *A Tale of Two Portals: Testing Light, Hidden New Physics at Future e^+e^- Colliders*, JHEP **06** (2017) 077 [`arXiv:1704.00730`] [INSPIRE].

[45] S. Dutta, D. Sachdeva and B. Rawat, *Signals of Leptophilic Dark Matter at the ILC*, Eur. Phys. J. C **77** (2017) 639 [`arXiv:1704.03994`] [INSPIRE].

[46] M. Duch, B. Grzadkowski and A. Pilaftsis, *Gauge-Independent Approach to Resonant Dark Matter Annihilation*, JHEP **02** (2019) 141 [`arXiv:1812.11944`] [INSPIRE].

[47] G. Cacciapaglia, A. Deandrea and S. De Curtis, *Nearby resonances beyond the Breit-Wigner approximation*, Phys. Lett. B **682** (2009) 43 [`arXiv:0906.3417`] [INSPIRE].

[48] Y. Kato, *Probing the dark sector via searches for invisible decays of the Higgs boson at the ILC*, in *2019 European Physical Society Conference on High Energy Physics*, (2020) [`arXiv:2002.12048`] [INSPIRE].

[49] J. de Blas et al., *Higgs Boson Studies at Future Particle Colliders*, JHEP **01** (2020) 139 [`arXiv:1905.03764`] [INSPIRE].

[50] INTERNATIONAL LARGE DETECTOR CONCEPT GROUP collaboration, *Search for Light Scalars Produced in Association with a Z boson at the 250 GeV stage of the ILC*, PoS **ICHEP2018** (2019) 630 [INSPIRE].

[51] Y. Wang, *Search for Extra Scalars Produced in Association with a Z boson at the ILC*, talk at *The International Workshop on Future Linear Colliders (LCWS) 2018*, Arlington, U.S.A., 22–26 October 2018.

[52] CLICDP collaboration, *Sensitivity to new physics scenarios in invisible Higgs boson decays at CLIC*, in *International Workshop on Future Linear Colliders*, (2020) [`arXiv:2002.06034`] [INSPIRE].

[53] A.L. Read, *Presentation of search results: The CL_s technique*, J. Phys. G **28** (2002) 2693 [INSPIRE].

[54] A. Denner, *Techniques for calculation of electroweak radiative corrections at the one loop level and results for W physics at LEP-200*, Fortsch. Phys. **41** (1993) 307 [`arXiv:0709.1075`] [INSPIRE].